

(2)

WL-TR-94-5005

AD-A279 157



OPTICAL PROCESSING AND CONTROL

ANDREW SUZUKI, DALE STEVENS, MIKE PRAIRIE
JAMES GROTE, ANTONIO CRESPO
JOSEPH BRANDELIK, SAMUEL ADAMS

JANUARY 1994

FINAL REPORT FOR 10/01/86-09/01/92

APPROVED FOR PUBLIC RELEASE; DISTRIBUTION IS UNLIMITED.

Solid State Electronics Directorate
Wright Laboratory
Air Force Materiel Command
Wright-Patterson Air Force Base, OH 45433-7331

DTIC
ELECTE
MAY 11 1994
S B D

94-13913



DTIC QUANTITY EDITION

Q88

94 5 09 005

NOTICE

WHEN GOVERNMENT DRAWINGS, SPECIFICATIONS, OR OTHER DATA ARE USED FOR ANY PURPOSE OTHER THAN IN CONNECTION WITH A DEFINITELY GOVERNMENT-RELATED PROCUREMENT, THE UNITED STATES GOVERNMENT INCURS NO RESPONSIBILITY OR ANY OBLIGATION WHATSOEVER. THE FACT THAT THE GOVERNMENT MAY HAVE FORMULATED OR IN ANY WAY SUPPLIED THE SAID DRAWINGS, SPECIFICATIONS, OR OTHER DATA, IS NOT TO BE REGARDED BY IMPLICATION, OR OTHERWISE IN ANY MANNER CONSTRUED, AS LICENSING THE HOLDER, OR ANY OTHER PERSON OR CORPORATION; OR AS CONVEYING ANY RIGHTS OR PERMISSION TO MANUFACTURE, USE, OR SELL ANY PATENTED INVENTION THAT MAY IN ANY WAY BE RELATED THERETO.

This report is releasable to the National Technical Information Service (NTIS). At NTIS, it will be available to the general public, including foreign nations.

This technical report has been reviewed and is approved for publication.

Joseph E. Brandelik

JOSEPH E. BRANDELIK, Sr. EE
E-O Techniques & Appl. Branch
Electro-Optics Division

John O. Crist

JOHN O. CRIST, Actg. Chief
E-O Techniques & Appl. Branch
Electro-Optics Division

C. Richard Lane

C. RICHARD LANE, Actg. Chief
Electro-optics Division
S. S. Electronics Directorate

If your address has changed, if you wish to be removed from our mailing list, or if the addressee is no longer employed by your organization please notify WL/ELOT, WPAFB, OH 45433-7331 to help us maintain a current mailing list.

Copies of this report should not be returned unless return is required by security considerations, contractual obligations, or notice on a specific document.

REPORT DOCUMENTATION PAGE

Form Approved
OMB No. 0704-0188

Public reporting burden for this collection of information is estimated to average 1 hour per response, including the time for reviewing instructions, searching existing data sources, gathering and maintaining the data needed, and completing and reviewing the collection of information. Send comments regarding this burden estimate or any other aspect of this collection of information, including suggestions for reducing this burden, to Washington Headquarters Services, Directorate for Information Operations and Reports, 1215 Jefferson Davis Highway, Suite 1204, Arlington, VA 22202-4302, and to the Office of Management and Budget, Paperwork Reduction Project (0704-0188), Washington, DC 20503.

1. AGENCY USE ONLY (Leave blank)	2. REPORT DATE	3. REPORT TYPE AND DATES COVERED	
	Jan 94	Final, Oct 86 - Sep 92	
4. TITLE AND SUBTITLE			5. FUNDING NUMBERS
Optical Processing and Control			PE 62204F PR 2001 TA 05 WU 10
6. AUTHOR(S) Andrew Suzuki, Dale Stevens, Mike Prairie, James Grote, Antonio Crespo, Joseph Brandelik, and Samuel Adams			8. PERFORMING ORGANIZATION REPORT NUMBER
7. PERFORMING ORGANIZATION NAME(S) AND ADDRESS(ES) E/O Techniques & Applications Branch WL/ELOT Bldg 22B, Suite 2 2700 D Street Wright-Patterson AFB OH 45433-7405			WL-TR-94-5005
9. SPONSORING/MONITORING AGENCY NAME(S) AND ADDRESS(ES) Solid State Electronics Directorate Wright Laboratory Air Force Materiel Command Wright-Patterson AFB OH 45433-7331			10. SPONSORING / MONITORING AGENCY REPORT NUMBER WL-TR-94-5005
11. SUPPLEMENTARY NOTES This is an in-house research report			
12a. DISTRIBUTION/AVAILABILITY STATEMENT Approved for public release, distribution unlimited		12b. DISTRIBUTION CODE	
13. ABSTRACT (Maximum 200 words) This report covers topics related to the Dember effect alignment of a ring laser gyro, measurement of the Fresnel drag coefficient, integrated optical switches, optically controlled superconductors and interrogation of fiber optic Bragg sensors. This report supplements prior in-house research efforts performed under this effort. (Reference AFWAL-TR-88-1050 and US patent 5, 258, 625). The work is being expanded and continued under in-house work unit 20010512.			
14. SUBJECT TERMS Superconductors, Matched Filters, Microwave Filters, Waveguides, Bragg Fiber Optics Sensors, Dember Effect			15. NUMBER OF PAGES 69
			16. PRICE CODE
17. SECURITY CLASSIFICATION OF REPORT UNCLASSIFIED	18. SECURITY CLASSIFICATION OF THIS PAGE UNCLASSIFIED	19. SECURITY CLASSIFICATION OF ABSTRACT UNCLASSIFIED	20. LIMITATION OF ABSTRACT UNLIMITED

FOREWORD

This is the final report on the in-house work unit 20010510. The work unit has been used to cover a variety of activities within the E-O Techniques & Applications Branch of the Electro-Optics Division, Solid State Electronics Directorate of the Wright Laboratory. The activities have included subject reviews in the literature, theoretical analysis of E-O related phenomena, and experimental research. The literature reviews have been conducted in preparation for subtopics for in-house research as well as potential future contractual effort. The major thrusts are reported in this document. The report covers efforts from October 1986 through September 1992. As of 1 October 1992, the work continuing under this effort is reported under in-house work unit 20010512.

The responsible program monitors have been successively Mike Prairie, James G. Grote, and Joseph E. Brandelik.

Accession For	
NTIS GRA&I	<input checked="" type="checkbox"/>
DTIC TAB	<input type="checkbox"/>
Unannounced	<input type="checkbox"/>
Justification _____	
By _____	
Distribution/ _____	
Availability Codes	
Distr	Avail and/or Special
A-1	

TABLE OF CONTENTS

<u>SECTION</u>	<u>TITLE</u>	<u>PAGE</u>
1.0	INTRODUCTION	1
2.0	RING LASER GYRO ALIGNMENT	3
	2.1 General References	4
3.0	THE DEMBER EFFECT	5
	3.1 References	9
4.0	FRESNEL DRAG COEFFICIENT MEASUREMENT	10
	4.1 Background	10
	4.2 Fresnel Drag in a Ring Laser	11
	4.2 Sagnac Effect	12
	4.3 Determination of α	12
	4-4 Experimental Results	13
	4.5 References	14
5.0	INTEGRATED OPTICAL SWITCHES	15
	5.1 Directional Coupler Switch	17
	5.2 Zero-Gap Directional Coupler Switch	20
	5.3 References	24
6.0	ALUMINUM GALLIUM ARSENIDE WAVEGUIDES	27
	6.1 References	31
7.0	FREDKIN GATES	32
	7.1 Digital Logic and the Fredkin Gate	33
	7.2 Optical Fredkin Gates	34
	7.3 References	36
8.0	OPTICALLY RECONFIGURABLE SUPERCONDUCTIVE CIRCUITS	39
	8.1 The Reconfigurable Electrical Device	41
	8.1.1 General References	54
	8.2 The Reconfigurable Magnetic Device	55
9.0	INITIAL INVESTIGATION OF AOTF & FOBG	57
	9.1 Background on Diffraction	59
	9.2 Acousto-Optical Tunable Filter (AOTF)	61

LIST OF FIGURES

<u>FIGURE</u>	<u>CAPTION</u>	<u>PAGE</u>
Figure 5-1:	Illustration of the Operation a Zero-Gap Directional Coupler Switch.	23
Figure 6-1:	Illustration of a Waveguide Structure.	29
Figure 6-2:	Illustration of Wafer Backside Etch Marks for Cleaving.	30
Figure 8-1:	Typical Type I Superconductor B Versus H Curve.	42
Figure 8-2:	Illustration of a Representative R_s Versus Temperature for a Type I Superconductor.	43
Figure 8-3:	Typical B Versus H Curve for a Type II Superconductor.	44
Figure 8-4:	Illustration of a Typical R_s Versus Temperature Curve for a Type II Superconductor.	45
Figure 8-5:	Illustration of Fringing Field Effects As Seen In a C/E versus W/h curve.	48
Figure 8-6:	Illustration of Field Pattern for Dual Microstrip Line Showing Even Mode Distribution.	50
Figure 8-7:	Illustration of Field Pattern for Dual Microstrip Line Showing Odd Mode Distribution.	50
Figure 8-8:	Illustration of Even Mode Capacitances for a Dual Transmission Microstrip.	51
Figure 8-9:	Illustration of Odd Mode Capacitances for a Dual Transmission Microstrip.	51
Figure 8-10:	Illustration of a Dual Transmission Microstrip Backward Wave Coupling Structure.	53
Figure 8-11:	Illustration of a Coupled Wave Transmission Line With "Interdigitated" Coupling.	56
Figure 9-1:	Section of a Reflection Grating.	60

LIST OF TABLES

<u>TABLE</u>	<u>TITLE</u>	<u>PAGE</u>
Table 4-1:	Fresnel Drag Coefficients.	13
Table 5-1:	Comparative Evaluation of Optical Integrated Circuits.	15
Table 5-2:	Substrate Materials Used for Optical Integrated Circuits.	16
Table 7-1:	Fredkin Gate Logic.	32

1.0 INTRODUCTION

The effort is divided into specific topics applicable to data processing. Those topics include the Dember effect, alignment of a ring laser gyro, measurement of the Fresnel drag coefficient, integrated optical switches, aluminum gallium arsenide waveguides, Fredkin gates, optically reconfigurable superconductive circuits, and an initial investigation into the application of an acousto-optical tunable filter (AOTF) to the interrogation of fiber optic Bragg sensors (FOBS)

Section 2.0 discusses the alignment of a ring laser gyro. This section represents primarily the work of James G. Grote and Samuel L. Adams. In part, the work was published in Optics & Technology Letters.

Section 3.0 discusses the Dember effect. Section 4.0 discusses the measurement of the Fresnel drag coefficient using a ring laser. In part, the work was published as AFWAL-TR-88-1050. Section 5.0 reviews integrated optical switches. Section 6.0 reviews aluminum gallium arsenide (AlGaAs) waveguides. Section 7.0 defines Fredkin gates. Sections 3, 4, 5, and 6 represents primarily the work of James G. Grote.

Section 8.0 discusses optically reconfigurable superconductive circuits. This section represents primarily the work of Andrew H. Suzuki and Joseph E. Brandelik. In part, the work is published as United States patent number 5,258,626 granted 2 Nov. 93 and United States patent number 5,287,302 granted 15 Feb. 94.

Section 9.0 discusses the application of amplitude modulated rf carriers in an AOTF for multiplexed signal interrogation of fiber optic Bragg sensors. This section represents primarily the work of Antonio Crespo and Dale Stevens. This report only presents the initial effort. The remainder of the effort is reported under in-house work unit 20010512 for project element 62204F.

2.0 RING LASER GYRO ALIGNMENT

Ring laser resonators require an auxiliary external to the cavity laser to achieve the critical alignment. The criticality of alignment arises from the requirement that the ring requires parallelism with the rotational plane of interest and the gyro requires central mirror alignment. Prior approaches have involved the use of an autocollimator in conjunction with the auxiliary laser. The approach utilized in the procedure described herein utilizes two auxiliary lasers and no collimator.

Each mirror mount requires six degrees of freedom to achieve the requisite alignment. A height gauge is utilized to set the height of a reference pinhole based on a transmissive reference auxiliary laser. Subsequently, the pinhole is placed in each leg of the ring laser and the mounts adjusted. Center alignment of each mirror is achieved by retro-reflection to the auxiliary laser through a pinhole. This procedure was repeated until all mirrors were uniformly illuminated. The front surfaces of the pinholes would now be at the center of rotation.

Subsequently, the helium neon plasma tube is introduced into the cavity. The tube was allowed to heat up for approximately one-half hour after which time it was essentially stabilized. The reference HeNe beam was then checked to insure alignment of the relative pinholes.

Next, the second auxiliary laser, beamsplitter assembly was placed into position. Then all the mirrors of the four leg resonator were aligned with this secondary reference to be at 45°. Then the second auxiliary laser & beamsplitter assembly were removed. At that point the ring laser starts to oscillate.

In summary, the first auxiliary establishes an initial alignment relative to the centers of the mirrors and the reference plane. The second auxiliary laser/beamsplitter combination provides sufficient resolution to allow the cavity to oscillate once the beamsplitter is removed.

2.1 General References

J. G. Grote and S. L. Adams, "Alignment procedure for a ring resonator cavity," Opt & Laser Tech. 21 (3) 169-172 (1989).

Z. -H. Fang and H. Thienpont, "Alignment technique for a ring cavity," Opt & Laser Tech. 16 269-270 (1984).

J. S. Uppal, J. C. Monga, and D. D. Bhawalkar, "A simple technique for the alignment of a ring resonator," Opt & Laser Tech. 17 215-216 (1985).

3.0 THE DEMBER EFFECT

In 1932, H. Von Dember observed the generation of an electromotive force (emf) between the illuminated and nonilluminated regions of a copper oxide crystal[1,2]. This is a photovoltaic effect now known as the dember effect. The Dember effect has been observed in various semiconducting crystals and has been used to study surface barrier properties of crystals.

If the illumination of a semiconductor surface is nonuniform, a nonuniform distribution of free carriers is formed in any quasineutral region (or diffusion region between unequal illumination regions). In such a diffusion region there is a gradient of nonequilibrium density of carriers. The diffusion currents give rise to the "Dember" emf.

Consider the one-dimensional theoretical construct[3]. The electron and hole current densities are given by:

$$j_n = en\mu_n E + eD_n \partial n / \partial x \quad (3-1)$$

and

$$j_p = ep\mu_p E + eD_p \partial p / \partial x \quad (3-2)$$

where e is the absolute value of the electronic charge, n and p are the concentrations of electrons and holes, respectively, μ_n and μ_p are the electron and hole mobilities, respectively, E is the internal electric field, and D_n and D_p are the electron and hole diffusion coefficients, respectively.

Using Einstein's equation[4,5] to relate the mobilities of carriers to their respective diffusion coefficients gives:

$$D_n = \mu_n kT/e \quad (3-3)$$

and

$$D_p = \mu_p kT/e \quad (3-4)$$

where k is Boltzman's constant, and T is the temperature in degrees Kelvin. Adding equations (3-1) and (3-2) and then substituting using equations (3-3) and (3-4), the total current is:

$$J = j_n + j_p = e(n\mu_n + p\mu_p)E + kT(\mu_n \partial n / \partial x - \mu_p \partial p / \partial x) \quad (3-5)$$

Under steady state conditions, with illumination and the external circuit open, $J = 0$. The electric field is then given by:

$$E = \left(\frac{kT}{e} \right) \frac{(\mu_n \partial n / \partial x) - (\mu_p \partial p / \partial x)}{n\mu_n + p\mu_p} \quad (3-6)$$

Assuming charge neutrality is conserved and that the local level charge is negligible or we are in the quasineutral region, $\Delta n = \Delta p$. Then, $\partial n / \partial x = \partial p / \partial x$. Equation (3-6) can then be written as:

$$E = \left(\frac{kT}{e} \right) \frac{(\mu_n - \mu_p)(\partial n / \partial x)}{n\mu_n + p\mu_p} \quad (3-7)$$

The bulk conductivity of the semiconductor is given as $\sigma_B = e(n\mu_n + p\mu_p)$. Partial differentiation of the bulk conductivity with respect to the x coordinate gives:

$$\frac{\partial \sigma_B}{\partial x} = \left(\frac{kT}{e}\right) (\mu_n - \mu_p) \left(\frac{1}{\sigma_B}\right) \left(\frac{\partial \sigma_B / \partial x}{\mu_n + \mu_p}\right) \quad (3-8)$$

After substituting the terms in equation (3-8) into equation (3-7) we obtain:

$$E = \left(\frac{kT}{e}\right) (\mu_n - \mu_p) \left(\frac{1}{\sigma_B}\right) \left(\frac{\partial \sigma_B / \partial x}{\mu_n + \mu_p}\right) \quad (3-9)$$

The potential difference between the illuminated region and the dark region of the semiconductor is:

$$V = - \int_{dark}^{illuminated} E dx = - \left(\frac{kT}{e}\right) \left(\frac{\mu_n - \mu_p}{\mu_n + \mu_p}\right) \frac{\sigma_{B_0}}{\sigma_{B_i}} \int_{B_i}^{B_0} \frac{1}{\sigma_B} dx = \\ - \left(\frac{kT}{e}\right) \left(\frac{\mu_n - \mu_p}{\mu_n + \mu_p}\right) \ln \left(\frac{\sigma_{B_i}}{\sigma_{B_0}}\right) \quad (3-10)$$

where $\sigma_{B_0} = e(n_0\mu_n + p_0\mu_p)$ is the conductivity of the semiconductor in the dark, and $\sigma_{B_i} = \sigma_{B_0} - \Delta\sigma$ is the conductivity of the semiconductor under illumination. n_0 and p_0 are equilibrium concentrations of free carriers in the neutral volume of the semiconductor. This potential difference, V, is the Dember emf.

Substituting $\sigma_{B_0} - \Delta\sigma$ for σ_{B_i} in equation (3-10) gives:

$$\ln\left(\frac{\sigma_{B_i}}{\sigma_{B_0}}\right) = \ln\left(\frac{\sigma_{B_0} - \Delta\sigma}{\sigma_{B_0}}\right) = \ln\left(1 + \frac{\Delta\sigma}{\sigma_{B_0}}\right) \quad (3-11)$$

Hence, it follows that:

$$V = -\left(\frac{kT}{e}\right)\left(\frac{\mu_n - \mu_p}{\mu_n + \mu_p}\right)\ln\left(1 + \frac{\Delta\sigma}{\sigma_{B_0}}\right) \quad (3-12)$$

From expressions (3-10) and (3-12), it can be seen that the Dember emf is proportional to the mobilities of the free carriers. The larger the difference between μ_n and μ_p , the higher the Dember emf. When the mobilities are equal, the Dember emf becomes zero.

For the case where $\Delta\sigma \ll \sigma_{B_0}$, equation (3-12) can be simplified by using the first term of the series expansion of the logarithm.

This gives:

$$V = -\left(\frac{kT}{e}\right)\left(\frac{\mu_n - \mu_p}{\mu_n + \mu_p}\right)\left(\frac{\Delta\sigma}{\sigma_{B_0}}\right) \quad (3-13)$$

Equation (3-13) shows that at low excitation levels the Dember emf between the illuminated and dark regions is directly proportional to the conductivities between these two regions. By increasing the average conductivity of the semiconductor, it is readily seen that the Dember emf will decrease. The decrease of the emf with the increase of conductivity can be explained as follows: The gradient produced by nonuniform illumination and the diffusion current, which is proportional to the gradient, produce an electrical field and a conduction current. Under steady state conditions, the diffusion current equals the conduction current. This means that the higher the conductivity, the lower the Dember emf.

This contradiction with the derivation of equation (3-10) is due to the assumption $\Delta n = \Delta p$ for the conservation of neutrality. In this case, the equations for current were used to derive the Dember emf, where, we can assume that $\Delta n \approx \Delta p$, because, the difference between these two quantities is negligible[6].

The Dember effect has been studied using many semiconducting materials and observed at metal-semiconductor interfaces[7]. The effect has been used to provide evidence for surface states on semiconductors using germanium and silicon surfaces[8].

3.1 References

1. H. Dember, *Zeitschrif Physik* 32, 554 (1932).
2. H. Dember, *Z. Physik* 32, 856 (1932).
3. W. Roosbroeck, *Phys. Rev.* 91, 282 (1953).
4. J. McKelvey, Solid State and Semiconductor Physics, (Robert E. Krieger Publishing Co., Malabar, Fl, 1986), Chapter 10.
5. V. A. Myamlin, Y. V. Pleskov, Electrochemistry of Semiconductors, (Plenum Press, New York, 1967), Chapter 1.
6. S. M. Ryvkin, Photoelectric Effects in Semiconductors, (Consultants Bureau, New York, 1964), Chapter 12.
7. J. Tauc, Photo and Thermoelectric Effects in Semiconductors, (Pergamon Press, Inc., New York, 1962), Chapter 3.
8. W. H. Brattain, *Phys. Rev.* 72, 345 (1947).

4.0 FRESNEL DRAG COEFFICIENT MEASUREMENT

The objective of this research was to improve the accuracy of the measurement of the Fresnel drag coefficient in a ring laser gyroscope over that reported by Bilger and Stowell[1].

Fresnel drag is manifest as a change in the speed of light passing through a transparent moving medium. The change is proportional to the refractive index and the velocity of the medium. The technique employed was to insert a transparent moving medium into a laser gyro cavity. The high quality (minimal scattering) mirrors provide the opportunity to improve the measurement over previous experiments.

4.1 Background

In 1818, Fresnel theorized the existence of the subject "drag" [2]. With $\alpha = 1 - (1/n^2)$ as the Fresnel drag coefficient, n the refractive index of the stationary medium, δV_1 is the change in velocity of the light through a transparent moving medium, and V_m is the velocity of the moving medium, then:

$$\delta V_1 = \left(1 - \frac{1}{n^2}\right) V_m \quad (4-1)$$

$$V_i = n(\lambda) V_r \quad (4-3)$$

where V_i is the component of V_m in the direction of the incident light and V_r is the component of V_m in the direction of the refracted light. For the case where V_m is parallel to the surface

normal to that of the moving medium and the incident light[3] we have: $V_i = V_r = V_m$. Based on that criteria a higher order dispersive term is introduced and we have:

$$\alpha_{La} = 1 - \left(\frac{1}{n^2}\right) - \left(\frac{\lambda}{n^2}\right) \left(\frac{\partial n}{\partial \lambda}\right) \quad (4-4)$$

Where α_{La} is the drag coefficient given by Laub. There have been many attempts to verify which coefficient was valid. Using a refined experiment, Bilger and Stowell concluded that the Lorentz equation was more accurate.

4.2 Fresnel Drag in a Ring Laser

Starting with the Post[4] equation for the beat frequency of a ring laser with a transparent moving media in the cavity:

$$\delta f_{BM} = \left(\frac{2f}{c}\right) \left(\frac{\oint n^2 \alpha V \cdot d\vec{r}}{\oint n d\vec{r}}\right) \quad (4-5)$$

where δf_{BM} is the beat frequency of the ring laser due to the moving medium, f is the frequency of the propagating beam, c is the velocity of light in a vacuum and $d\vec{r}$ is the line element along the beam path. From that one can derive the following[5]:

$$\delta f_{BM} = 2lV_m \left(\frac{n^2 - 1}{L\lambda}\right) \quad (4-6)$$

where l is the length of the moving medium and L is the optical path length of the cavity including the moving medium. Using a rotating cylinder, equation 4-6 becomes:

$$\delta f_{BM} = \frac{4\pi n^2 \alpha f_m l X_o}{L\lambda \tan(\beta)} \quad (4-7)$$

where $f_m = V_m/2\pi$ is the rotational frequency of the moving medium, x_0 is the horizontal displacement of the light beam from the axis of rotation of the moving medium, and θ is the angular displacement of the face of the moving medium from normal incidence to the light beam. The angular displacement is about the horizontal axis.

4.2 Sagnac Effect

The Sagnac effect arises because of the earth's rotation. This requires that effect be added to equation 4-5 to give the total beat frequency as:

$$\delta f_B = \delta f_{Bm} + \delta f_{Bs} \quad (4-8)$$

where:

$$\delta f_{Bs} = \frac{4A\Omega \sin(\theta)}{L\lambda} \quad (4-9)$$

is the beat frequency due to the Sagnac effect. Based on the latitude, $\theta = 39^\circ 47' 1.5''$, at Wright-Patterson AFB, $\delta f_{Bs} = 78.25 \pm 0.13$ Hz.

4.3 Determination of α

The drag coefficient is determined from the slope of the ratio of the beat frequency, δf_B , to the rotational frequency of the moving medium, f_m . With $R = \partial \delta f_B / \partial f_m$ is the slope of the ratio of the beat

frequency to the rotational frequency of the moving medium, we have:

$$\alpha = R \left(\frac{L \lambda \tan(\beta)}{4 \pi n^2 l X_0} \right) \quad (4-10)$$

Also, $R = \partial \delta f_B / \partial f_m$ is the slope of the ratio of the beat frequency to the displacement of the moving medium from the center of rotation. Using equation 4-10, equation 4-8 can be written as $\delta f_B = R f_m + \delta f_{Bs}$.

If β is set to Brewster's angle, equation 4-7 reduces to:

$$\delta f_{bm} = \frac{4 \pi n \alpha f_m l X_0}{L \lambda} \quad (4-11)$$

where $\tan(\beta) = n$ (the index of refraction).

4-4 Experimental Results

The Fresnel drag coefficient (α) was determined from the experimental data[7] as shown in Table 4-1.

Table 4-1: Fresnel Drag Coefficients.

Coefficient Symbol	Coefficient Value	\pm % Error
α_{fm}	0.352	2.8
α_{X_0}	0.360	3.3
α_{exp}	0.356	4.3
α_{Lo}	0.541609	0.0007
α_{La}	0.537648	0.0007

The large errors are attributed to the bandwidth of the filter used to determine the beat frequency. In retrospect, the filter should have been narrower and optimized for each measurement. Time constraints precluded correction of the experimental procedure and measurements to achieve higher accuracy.

4.5 References

1. H. R. Bilger and W. K. Stowell, "Light Drag in a Ring Laser: An Improved Determination of the Drag Coefficient," Phys. Rev. A 16 (1) 313 (1977).
2. H. A. Lorentz, The Theory of Electrons and its Applications to the Phenomena of Light and Radiant Heat, 2ed, Dover Publications, New York, NY 1952.
3. W. F. Parks and J. T. Dowell, "Fresnel Drag in Uniformly Moving Media," Phys. Rev. A 9 (1) 565 (1974).
4. E. J. Post, "Sagnac Effect," Rev. Mod. Phys. 39 475 (1967).
5. W. M. Macek, J. R. Schneider, and R. M. Salamon, "Measurement of Fresnel Drag With the Ring Laser," J. Appl. Phys. 35 2556 (1964).
6. H. R. Bilger and A. T. Zavodny, "Fresnel Drag in a Ring Laser: Measurement of the Drag Coefficient," Phys. Rev A 5 (2) 591 (1972).
7. James G. Grote, Precision Measurement of the Fresnel Drag Coefficient Using a Ring Laser, AFWAL-TR-88-1050, May 1988.

5.0 INTEGRATED OPTICAL SWITCHES

Since the development of the first lasers in the 1960's, there has been a desire by the optical community to transmit and process signals using optical beams rather than electrical currents or radio waves. In the late 1960's, the concept of integrated optics emerged. In integrated optics, the through-the-air optical paths and conventional electrical integrated circuits are replaced by miniaturized optical integrated circuits (OIC's).

Table 5-1: Comparative Evaluation of Optical Integrated Circuits[1].

Potential Advantages
Increased Bandwidth
Expanded Frequency (Wavelength) Division Multiplexing
Low-Loss Couplers, Including Bus Access Types
Expanded Multipole Switching (Number of Poles, Switching Speed)
Smaller Size, Weight, Lower Power Consumption
Batch Fabrication Economy
Improved Reliability
Improved Optical Alignment, Immunity to Vibration
Fabrication Compatibility With Electronics
Major Disadvantages
High Cost of Developing New Fabrication Technology
Lack of Maturity With Active Materials

The optical integrated circuit has a number of potential advantages when compared to either its counterpart, the electrical integrated circuit, or to conventional optical signal processing systems composed of relatively large discrete elements.

There are two basic forms of optical integrated circuits, hybrid and monolithic. In the hybrid approach, two or more substrate materials are somehow bonded together to optimize the performance for different devices. In the monolithic approach, a single substrate material is used for all devices. Since OIC's require a light source, at some point in the circuit, active materials are required. Therefore, true monolithic circuits can only be fabricated in optically active material.

Table 5-2: Substrate Materials Used for Optical Integrated Circuits.

Passive	Active
Quartz	Gallium Arsenide
Lithium Niobate	Gallium Aluminum Arsenide
Lithium Tantalate	Gallium Arsenide Phosphide
Tantalum Pentoxide	Gallium Aluminum Nitride
Niobium Pentoxide	Indium Phosphide
Silicon	Other III-V, II-VI, etc.

Table 5-2 lists some of the materials under consideration. While still in its infancy, the optical grade polymers appear to offer promise as substrate, active and passive waveguides, and as sources.

A detailed analysis of integrated optical waveguide propagation is provided by several authors and will not be repeated here[1,2].

A primary component of any optical switch is a coupler between waveguides. There are many types of couplers between waveguides. Coupling between two planar waveguides can occur by "tunneling" through the separation medium into the adjacent guide. Such tunneling requires that the evanescent waves "tails" of the two waveguides overlap.

The dual-channel directional coupler, which is analogous to the microwave dual guide multihole coupler[3] consists of parallel channel optical waveguides sufficiently closely space so that the energy is transferred from one to the other by tunneling.

Modulation of light in integrated optics falls into three categories. Namely, "resonant" absorption, switching between two waveguides, and phase modulation of a single waveguide. All methods have been demonstrated at frequencies in excess of 100 GHz. Unfortunately, the modulation depth at the higher frequencies is only a few percent. Resonant absorption can manifest itself as electro-optical absorption through the Franz-Keldysh effect. Switching modulation can manifest itself in the form of a Mach-Zehnder interferometer. Phase modulation includes basic retardation of the phase and, hence, requires an unmodulated reference. Phase modulation by a change in polarization alleviates the reference requirement. Polarization modulation is achieved by introducing a linearly polarized optical beam at 45° to the x and y axes. Since phase change would occur for only one dimension (x or y), the polarization vector is effectively rotated.

With interlaced electrodes on an electro-optically active material, one can generate a Bragg effect "directional" modulator by varying the field between the electrodes. The linear electro-optic effect can be used to reduce the index of refraction of a layer of the waveguide thereby allowing a total internal reflection of the optical beam[4].

5.1 Directional Coupler Switch

The directional coupler switch is a device consisting of parallel channel waveguides separated by a finite distance. The coupling between the modes of the parallel waveguides results in an exchange of power between guided modes of adjacent waveguides. This is referred to as directional coupling. The eigenmodes of the coupling

region consist of one symmetric and one antisymmetric mode. Treatment of waveguide coupling can be performed by coupled-mode theory to give the power from the output waveguides of the directional coupler[5-8]. Consider P_{i_1} as input channel 1, P_{i_2} as input channel 2, P_{o_1} as output channel 1 and P_{o_2} as output channel 2. Let waveguide 1 propagate through the symmetric mode and waveguide 2 propagate through the antisymmetric mode. Also, assume that the waveguides are not too close so, then, the overlap integral of the mode functions will be small. With a single input to waveguide P_{i_1} , $P_{i_2} = 0$, the output power from guides P_{o_1} and P_{o_2} are, respectively, given as:

$$P_{o_1}(l) = P_{i_1} - P_{o_2}(l) \\ = P_{i_1}(1 - (\kappa^2 / (\kappa^2 + \delta^2))(1 - \cos^2[(\kappa^2 + \delta^2)^{1/2}l])) \quad (5-1)$$

$$P_{o_2}(l) = P_{i_1}((\kappa^2 / (\kappa^2 + \delta^2))(\sin^2[(\kappa^2 + \delta^2)^{1/2}l])) \quad (5-2)$$

where $2\delta = \beta_1 - \beta_2$ is the difference in the propagation constants between two adjacent uncoupled waveguides, named here waveguide 1 and waveguide 2, κ is the coupling constant between the two adjacent waveguides, and l is the interaction length over which the two waveguides are coupled. By definition, $\kappa = \pi/2L$, where $l = L$ is the length required for complete coupling of the power from one waveguide to the other.

For symmetric waveguides the phase velocities in the two modes are equal, i.e., $\beta_1 = \beta_2$ or $\delta = 0$. For $\delta = 0$ and $l = L$, equations (5-1) and (5-2) become:

$$P_{o_1}(L) = P_{i_1}(1 - 1(1 - \cos^2[\pi/2])) = 0 \quad (5-3)$$

$$P_{o_2}(L) = P_{i_1}(\sin^2[\pi/2]) = P_{i_1} \quad (5-4)$$

From equations (5-3) and (5-4), one can see that the input power into waveguide 1, P_{i_1} , will exit waveguide 2, P_{o_2} , at a distance $l = L$. The distance for complete power transfer from one mode to the

other will occur at $L = \pi/2\kappa$.

Applying an electric field to either waveguide 1 or waveguide 2, over the distance L , where the waveguides are coupled, will change that waveguides propagation constant β . Total switching then occurs when $\delta = \sqrt{3}\kappa$ [5,8]. This can be verified by the substitution of $\delta = \sqrt{3}\kappa$, along with $\ell = L$, into equations (5-1) and (5-2) where we get:

$$P_{O_1}(L) = P_{i_1}(1 - (1/4)(1 - \cos^2[\pi])) = P_{i_1} \quad (5-5)$$

$$P_{O_2}(L) = P_{i_1}((1/4)(\sin^2[\pi])) = 0 \quad (5-6)$$

Using the definitions for 2δ and κ , one gets total switching to occur when:

$$(\beta_1 - \beta_2) = \sqrt{3}\pi/L \quad (5-7)$$

By definition, $\beta = 2\pi n/\lambda$, where n is the refractive index of the waveguiding material and λ is the wavelength of the source[5-7]. To apply an electric field to one of the waveguides we must place electrodes on top of waveguides 1 and 2 over the coupling length L . Applying a voltage V to the electrode over, say, waveguide 2 will produce a change in the refractive index n_2 by an amount proportional to that voltage. This is mathematically given by:

$$n_2 = (1/2)n_2^3 r V \quad (5-8)$$

where r is the electro-optic coefficient of the waveguiding material and V is the applied voltage[5-7]. Substitution of equation (5-8) into (5-7), using the definition for β , gives:

$$(2\pi/\lambda)(n_1 - (1/2)(n_2^3 r V)) = \sqrt{3}\pi/L \quad (5-9)$$

We can now find the voltage required to completely switch the coupling: From equation (5-9) we determine:

$$V = (2/n_2^3 r) (n_1 - \sqrt{3}\lambda/2L) \quad (5-10)$$

The applied voltage V required to produce a $\pi/2$ change in δ is known as the half wave voltage V_* .

An additional parameter that needs to be considered for directional couplers is wavefront tilt and its affect on waveguide coupling in the branching section. The larger the tilt angle α of the branching section, the less the waveguide coupling[7]. Tilt introduces phase differences that decrease waveguide interaction in the branching section of waveguide coupling. The maximum allowable tilt angle can be obtained by forcing the branching region of waveguide coupling to be within a single lobe of the standing wave generated by the two waves propagating along the tilted waveguide portions[7]. This gives the limit:

$$\sin(\alpha/2) < \lambda/4nw \quad (5-11)$$

where α is the tilt angle of the branching section and w is the width of the waveguides.

5.2 Zero-Gap Directional Coupler Switch

As in directional couplers, the interaction region of a zero-gap directional coupler will support two guided symmetric modes and two guided antisymmetric modes. The difference between them, however, comes from the fact that we have zero spacing between the two symmetric waveguides in a zero-gap directional coupler, so these modes will now be propagating in a single waveguide. We will again have a voltage independent phase difference that accumulates over the interaction length, the two mode section, due to the difference in the phase velocities of the two orthogonal modes, and a phase difference over the two mode section brought about by the electro-optic effect.

The electro-optic dependent phase difference will be denoted by $(\beta_s - \beta_{as})/2 = \Delta\beta/2$, where β_s and β_{as} are the propagation constants of the symmetric and antisymmetric modes, respectively. The value of $\Delta\beta$ required for complete coupling of energy from the top half of the two mode waveguide to the bottom is given by[9]

$$\Delta\beta = \pi/L \quad (5-12)$$

where $\Delta\beta$ is varied by changing the index of refraction of the waveguiding material in the two mode section. We will denote the refractive index change by Δn . The change in the difference between the propagation constants of the two modes can then be written as[9]:

$$\Delta(\Delta\beta)/\Delta n = \partial\Delta\beta/\partial n \quad (5-13)$$

Equating equations (5-12) and (5-13) gives:

$$\Delta n = (\pi/L)(\partial\Delta\beta/\partial n)^{-1} \quad (5-14)$$

For linear electro-optic materials the refractive index changes proportionally to the applied voltage. With this relation, it can be seen from equation (5-14) that $\partial\Delta\beta/\partial n$ is inversely proportional to the applied voltage. This ratio, $\partial\Delta\beta/\partial n$, is strongly dependent on the waveguide separation s for the directional coupler[5,9]. The value of $\partial\Delta\beta/\partial n$ increases as s decreases and as $\partial\Delta\beta/\partial n$ increases, V decreases. Therefore, the maximum value of $\partial\Delta\beta/\partial n$ and, thus, the minimum voltage V required to switch the coupling guides, occurs when $s = 0$. When $s = 0$ we have a zero-gap directional coupler. Experiments have already shown that the value $\partial\Delta\beta/\partial n$ varies by an order of magnitude between the conventional directional coupler and the zero-gap directional coupler[9]. This verifies that zero-gap directional couplers require less voltage to switch the coupling than do conventional directional couplers.

Expressions for the power coupling in zero-gap directional couplers are similar to those for conventional directional couplers. They are given by [5-7,10-17]:

$$P_{O_1}(t) = P_i \cos^2[(\Delta\beta/2 + \Phi_0)t] \quad (5-15)$$

$$P_{O_2}(t) = P_i \sin^2[(\Delta\beta/2 + \Phi_0)t] \quad (5-16)$$

where Φ_0 is the accumulated, voltage independent, phase difference in the phase velocities of the symmetric and antisymmetric modes. These expressions are the essentially same ones given for the conventional symmetric direction coupler when $\delta = 0$, except that κ has been substituted by $\Delta\beta/2$. Now, for the zero-gap directional coupler, coupling occurs at $\Phi_0 = \pi/2L$, $\Delta\beta = 0$, and switching occurs at $\Delta\beta = \pi/L$. The applied voltage required to switch the coupling is, thus, given by:

$$V = (\lambda/n^3 r L) \quad (5-17)$$

where n is the refractive index of the interaction region. The applied voltage required to produce a $\pi/2$ change in $\Delta\beta/2$ is, again, referred to as the half wave voltage V_s .

Figure 5-1a shows operation with no voltage applied, while Figure 5-1b shows operation with a voltage applied to the electrode over waveguide 2.

The separation gap g between the electrodes over the coupling regions of waveguide 1 and waveguide 2, even though not being part of the equations above, plays a major role in switch operation. It has been found that the wider the gap, the lower the electric field strength and induced refractive index change, and the narrower the gap, the higher the electric field strength and induced refractive index change[18]. It has also been presented that the electrode separation gap depends on the waveguide width w and should be much less than the waveguide width so that only the propagation constant

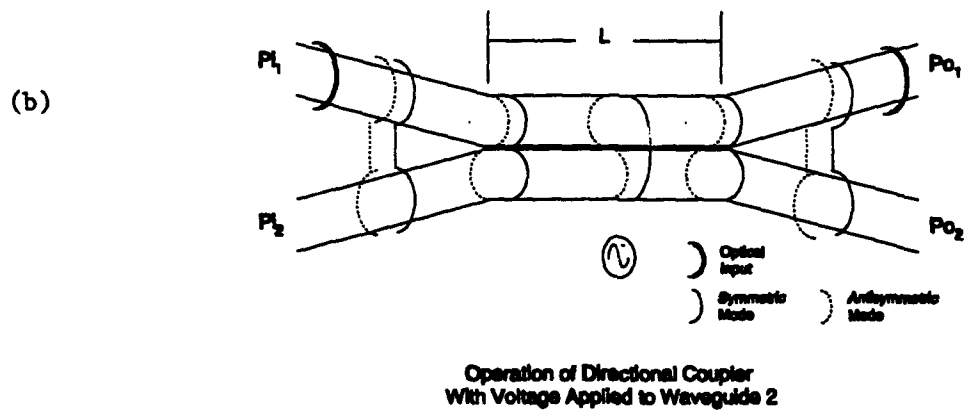
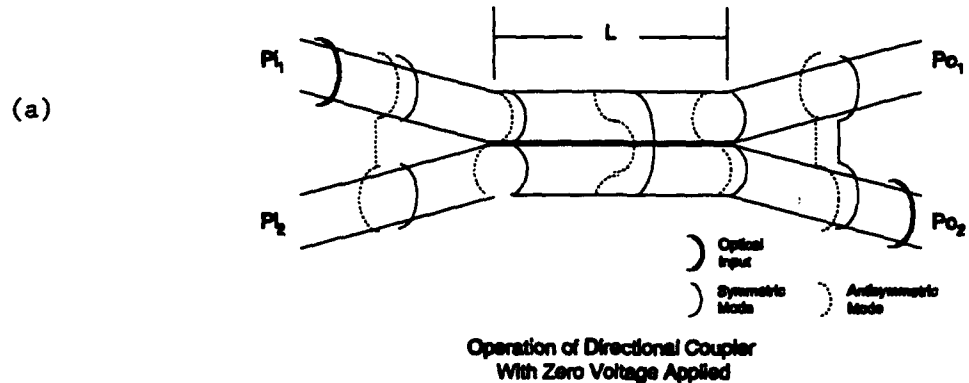


Figure 5-1: Illustration of the Operation a Zero-Gap Directional Coupler Switch.

of the fundamental mode is strongly modified[15,18]. There are limitations, however, on how narrow or wide g can be. This is due to the physical reason that variations in the electrode gap can only partially be compensated by applied voltage. Complete compensation is not possible because overlap of the applied electric field with the optical electric field within the waveguide, brought about by the electrode separation gap versus applied voltage, are factors that affect the behavior of the index change. This leads to the need to determine an optimum g versus waveguide width [18].

5.3 References

1. Robert G. Hunsperger, Integrated Optics: Theory and Technology, 2ed, (Springer-Verlag, New York, NY 1985).
2. T. Tamir, Integrated Optics, 2ed, Topics in Appl. Phys 7, (Springer, New York 1979).
3. A. L. Lance, Introduction to Microwave Theory and Measurements (McGraw-Hill, New York 1964) 116-117.
4. C. S. Tsai, B. Kim, F. R. El-Allaro, IEEE J Quantum Electron. QE-14 513 (1978).
5. A. Yariv and P. Yeh, Optical Waves in Crystals, John Wiley and Sons, New York, NY, 1984.
6. D. L. Lee, Electromagnetic Principles of Integrated Optics, John Wiley and Sons, New York, NY, 1986.
7. R. A. Forber and E. Marom, "Symmetric Directional Coupler Switches," IEEE Journal of Quantum Electronics, Vol. QE-22, 911, (1986).
8. M. J. Robertson, S. Ritchie and P. Dayan, "Semiconductor Waveguides: Analysis of Optical Propagation in Single Rib Structures and Directional Couplers," IEE Proceedings, Vol. 132, Pt. J, 336, (1985).
9. M. Papuchon and Am. Roy, "Electrically Active Optical Bifurcation: BOA," Applied Physics Letters, Vol. 31, 266, (1977).

10. K. Goel and W. S. C. Chang, "Extinction Ratio Degradation Due to Asymmetry in Zero-Gap Directional Coupling and Crossing Channel Switches," IEEE Journal of Quantum Electronics, Vol. QE-23, 2216, (1987).
11. K. Goel and W. S. C. Chang, "Design Considerations for Crossing Channel Switches," IEEE Journal of Quantum Electronics, Vol. QE-25, 47, (1989).
12. K. Goel, E. Wooten and W. S. C. Chang, "Design Considerations for Low Switching Voltage Crossing Channel Switches," Journal of Lightwave Technology, Vol. 6, 881, (1988).
13. R. A. Forber and E. Marom, "Optimization of Symmetric Zero-Gap Directional Couplers for Large Switch-Array Applications," Conference of Lasers and Electro-Optics Technology Digest, 288, (1985).
14. S. Gevorgyan and A. Hovsepyan, "Power Distribution in Symmetric Integrated Optic X Junction," Electronics Letters, Vol. 26, 788, (1990).
15. A. Neyer, "Electro-Optic X-Switch Using Single-Mode Ti:LiNbO₃ Channel Waveguides," Electronics Letters, Vol. 19, 553, (1983).
16. F. Rottmann, A. Neyer, W. Mevenkamp and E. Voges, "Integrated-Optic Wavelength Multiplexers on Lithium Niobate Based on Two-Mode Interference," Journal of Lightwave Technology, Vol. 6, 946, (1988).
17. C. De Bernardi, S. Morasca, C. Rigo, B. Sordo, A. Stano, I. R. Croston and T. P. Young, "Two Mode Interference Wavelength Demultiplexer Monolithically Integrated on InP, For 1.5 or 1.3 μm Operation," SPIE Journal of the 5th European Conference on Integrated Optics: ECIO '89, Vol. 1141, 238, (1989).

18. G. E. Betts and W. S. C. Chang, "Crossing-Channel Waveguide Electrooptic Modulators," IEEE Journal of Quantum Electronics, Vol. QE-22, 1027, (1986).

6.0 ALUMINUM GALLIUM ARSENIDE WAVEGUIDES

As electronic and optical data processing circuits approach multi-gigahertz operation rates, the need for multigigahertz communication between these processing circuits becomes essential. This communication includes chip-to-chip on a common multichip module, multichip module-to-multichip module on a common board, as well as board-to-board through a common backplane. The data rates at which communication through electrical interconnects can be transmitted is limited to the low gigahertz rates, unless one is willing to expend large amounts of power. This results from the fact that electrical wires and striplines possess frequency dependent dissipative losses due to conductive and dielectric properties, and frequency dependent parasitic coupling losses due to radiative and surface wave propagation properties[1]. The higher the frequency, the higher the losses. This is where optics can provide solutions. Optical interconnects can transmit data at optical frequencies with orders of magnitude lower losses than their electrical counterparts. In addition to the higher bandwidth and lower power consumption, they offer isolation from electromagnetic interference (EMI)[2].

Optical interconnects are starting to be utilized in chassis-to-chassis and board-to-board communication using glass optical fibers. On the smaller scale of multichip modules, and within chip, integrated optics is just beginning to emerge. Integrated optics offers the additional advantages of smaller interconnect widths and in-plane crossover capability with very low crosstalk and eliminating the need for air bridges. Thus, less wafer and board real estate will be required for optical interconnections, providing room for additional circuits and devices. Fabrication processes for integrated optics must be compatible with those used for the manufacture of electronic interconnects and devices. This is important from the standpoints of practicality and acceptability. AlGaAs/GaAs, as well as other III-V semiconductors,

is an attractive material because one can fabricate in it not only electronic integrated circuits, but laser sources, detectors, opto-electronic integrated circuits, optical modulators, and optical waveguides. AlGaAs/GaAs also possesses strong electro-optical effects which can be utilized to fabricate optical switches.

Optical switches can be incorporated with optical waveguides and other optical switches to realize digital logic operations or, very importantly, reconfigurable interconnects. Current research to develop processing techniques for AlGaAs/GaAs optical waveguides and devices has shown that the processing techniques for these optical circuits are compatible with the techniques used for the fabrication of electronic circuitry in GaAs. However, the regrowth techniques required for the lowest loss waveguides reduce the performance of electronics. Therefore, using AlGaAs/GaAs, one can house the entire electronic/pto-electronic circuit on a single substrate. The multichip module or board, now entirely electronic, could, with the incorporation of AlGaAs/GaAs opto-electronic circuits and optical waveguides, perform more efficiently, with less power consumption, move data around faster with less noise and use less real estate.

An even more attractive benefit is the potential to reconfigure the multichip modules to either perform entirely different operations, or to route signals around inoperative or defective portions of the module. Reconfigurable optical interconnects is an area that the United States Air Force is very much interested in.

Integrated optical circuit fabrication techniques are currently being explored for AlGaAs optical waveguides within the Wright Laboratory Solid State Electronics Directorate. AlGaAs layers have been using Molecular Beam Epitaxy (MBE) in the Directorate's Research Division. The structure being employed has $\text{Al}_{0.30}\text{Ga}_{0.70}\text{As}$ for the core and $\text{Al}_{0.35}\text{Ga}_{0.65}\text{As}$ for the cladding (Figure 6-1).

If the natural cleave lines are etched into the back of a GaAs

Figure 1

Waveguide Geometry

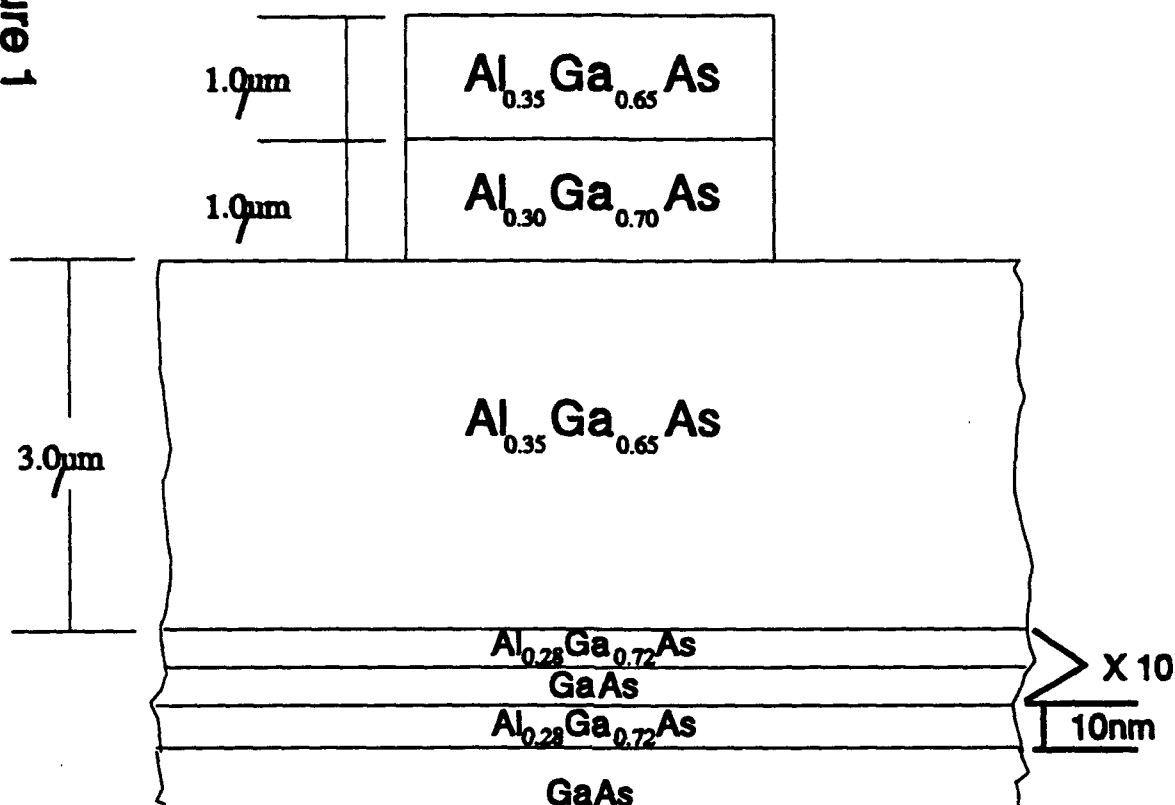


Figure 6-1: Illustration of a Waveguide Structure.

waver, they can be used to break the waveguide. Waveguide length cut-back is the standard technique employed to determine waveguide losses. The normal technique involves scribing and breaking. Since scribed lines are not in perfect alignment with natural cleave lines, there is an unwanted edge surface roughness that further complicates loss measurements. If the surface is metallized prior to etching, an infrared mask aligner can be used to precisely align the waveguides and cleave lines (Figure 6-2).

OPTICAL PROCESSING TECHNOLOGY

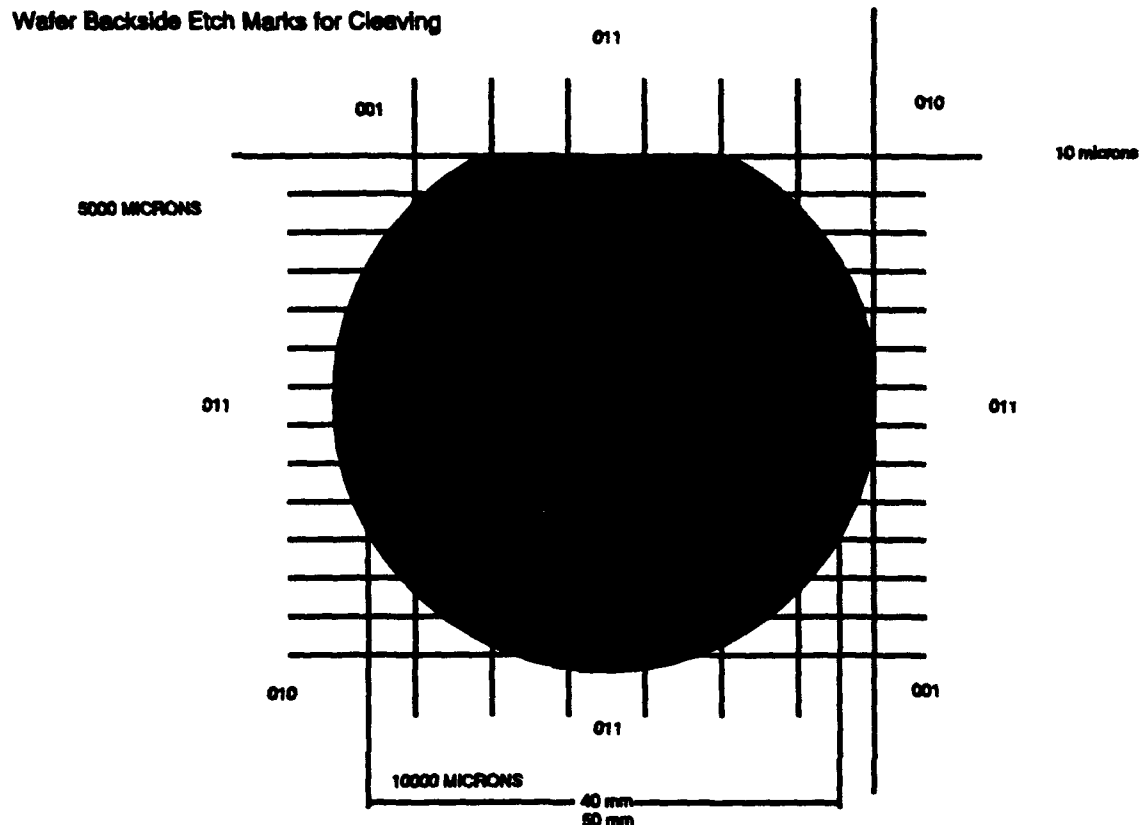


Figure 6-2: Illustration of Wafer Backside Etch Marks for Cleaving.

It is known that the preferential cleave planes are 011, 101, and 110. Use of the 001 direction for the waveguide light propagation would result in a diagonal plane at the input and output, since, GaAs cleaves easiest along the 110 plane for this orthogonal direction. Therefore, the 101 plane is best for waveguide propagation.

6.1 References

1. T. C. Edwards, Foundations for Microstrip Circuit Design, John Wiley and Sons, New York, NY, 1985.
2. J. W. Goodman, F. I. Leonberger, S-Y Kung and R. A. Athale, "Optical Interconnections for VLSI Systems," Proceedings of the IEEE, Vol. 72, 850, (1984).

7.0 FREDKIN GATES

Fredkin gate is a term given to a nonlinear dual input, dual output signal processing gate that performs a conditional crossover of the two input signals via an input control signal[1]. When the input control signal is a logic high, the two input signals follow a parallel path. When the input control signal is a logic low, the two input signal cross over. The logic of the Fredkin gate can, thus, be represented by Table 7-1.

Table 7-1: Fredkin Gate Logic.

u	x_1	x_2	v	y_1	y_2
0	0	0	0	0	0
0	0	1	0	1	0
0	1	0	0	0	1
0	1	1	→	1	1
1	0	0	1	0	0
1	0	1	1	0	1
1	1	0	1	1	0
1	1	1	1	1	1

Fredkin gates form the element on which conservative logic is based. Conservative logic is any Boolean function that is invertible and conservative. By invertible we shall not require invariance under time reversal, and, by conservative we shall require only that the model for computation possess at least one additive conserved quantity. Conserved quantities, such as conservation of energy, momentum, and angular momentum, are

functions of the system's state that remain constant. With conservative logic it is ideally possible to build sequential circuits that dissipate no internal power. Where the two input NAND gate forms the universal primitive for the set of all Boolean functions, the two input, two output, Fredkin gate forms the signal processing universal primitive for the set of all conservative logic functions.

7.1 Digital Logic and the Fredkin Gate

Often the functions we seek are nonreversible. These include elementary Boolean functions, such as AND and OR, as well as more complex functions, such as adders and flip flops[1-4]. By supplying constants along with the arguments to one or more Fredkin gates, one can realize many of these noninvertible functions using conservative logic. Conservative logic can be realized by AND, OR and NAND functions. J-K flip flops can be used to realize conservative logic. For almost all Boolean functions the number of gates increases exponentially with the number of input lines and, thus, the number of "don't cares" at the output also increase exponentially. This results in an exponential growth in dissipated energy. Conservative logic reduces the degree of dissipated energy growth over non-conservative logic, since, the number of gates does not depend on the number of inputs. For conservative logic, energy dissipation has linear growth[1-3]. This reduction in the dissipation of energy is achieved with the introduction of inverse conservative logic.

Inverse conservative logic is attained by replacing the conservative logic gate with its inverse. The Fredkin gate is attractive because it coincides with its inverse. An inverse looks like a mirror image of the original. By joining the original

function with its inverse, i.e., by connecting the outputs of the original Fredkin gate network to the inputs of the inverse Fredkin gate network, one will get back the original arguments and constants.

7.2 Optical Fredkin Gates

An optical Fredkin gate is the optical realization of the Fredkin gate with the use of an optical switch. The argument channels of the optical Fredkin gate are optical. However, the control channel for these devices can be either optical, electrical, or acoustical. Therefore, the optical Fredkin gate need not be entirely optical. It, also, does not have to operate exactly as Fredkin proposed. While some of the optical switch designs do switch the argument channels with a logic low control channel, Fredkin gate, other designs switch the argument channels with a logic high control channel. We will designate this type of gate as a reverse Fredkin gate, which is not the same as an inverse Fredkin gate.

Optical Fredkin gates have been proposed and demonstrated by several researchers utilizing various optical switching designs and materials[2-12]. Proposed optical implementations of the Fredkin gate include the polarization switch, acousto-optic gate, photorefractive gate, and waveguide switch.

Polarization switch, where the polarizations of the two arguments are orthogonal and are passed through an electro-optic modulator controlled by an applied electric voltage. This is a reverse Fredkin gate design. When voltage is applied to the modulator the polarizations of both arguments rotate by 90°, thus switching occurs. A similar method has been demonstrated using a polarization-color coded liquid crystal light valve.

Acousto-optic gate, where the arguments are passed through an

acousto-optic deflector and the control line is an acoustic signal applied to the deflector. This is also a reverse Fredkin gate design. Switching occurs in the presence of the acoustical signal.

Photorefractive gate, based on four wave mixing, is an all optical switch where the arguments are signal beams counterpropagated through a photorefractive material and the control line is the pump, also counterpropagated through the photorefractive material. This is, again, a reverse Fredkin gate design. When the pump is present, switching occurs via phase conjugation.

Waveguide switch, where the arguments are symmetric coupled channel waveguides in an electro-optically active material and, depending upon the extent of the optical activity of the material, the control channel is either an electrical or optical signal applied across the section of the two argument channels where coupling occurs.

Some of the designs for waveguide switches include: directional coupler switch; zero-gap directional coupler switch, which is a modified version of the directional coupler switch; and crossing channel switch or X-switch. The directional coupler switch designs operate as Fredkin gates where the X-switch designs operate as reverse Fredkin gates.

To be reported at a latter date under in-house work unit 20010512 will be an investigation of the channel waveguide zero-gap symmetric directional coupler switch. Researchers have thoroughly investigated the theory behind channel waveguide directional coupler switches and several of these devices have been demonstrated using lithium niobate (LiNbO_3), GaInAsP/InP and AlGaAs/GaAs as the waveguiding medium[12-25].

7.3 References

1. E. Fredkin and T. Toffoli, "Conservative Logic," International Journal of Theoretical Physics, Vol. 21, 219, (1982).
2. R. Cuykendall and D. R. Anderson, "Reversible Optical Computing Circuits," Optics Letters, Vol. 12, 542, (1987).
3. R. Cuykendall, "Three-Port Reversible Logic," Applied Optics, Vol. 27, 1772, (1988).
4. R. Cuykendall and D. McMillin, "Control-Specific Optical Fredkin Circuits," Applied Optics, Vol. 26, 1959, (1987).
5. J. Shamir, H. J. Caulfield, W. Micelli and R. J. Seymour, "Optical Fredkin Gate," SPIE Journal on Optical Computing, Vol. 625, 2, (1986).
6. J. Shamir, H. J. Caulfield, W. Micelli and R. J. Seymour, "Optical Computing and the Fredkin Gates," Applied Optics, Vol. 25, 1604, (1986).
7. K. M. Johnson, M. R. Surette and J. Shamir, "Optical Interconnection Network Using Polarization-Based Ferroelectric Liquid Crystal Gates," Applied Optics, Vol. 27, 1727, (1988).
8. E. M. Dianov, A. A. Kuznetsov, S. M. Nefjodov and G. G. Voevodkin, "Optical Realization of Fredkin Gates Matrix Using Liquid Crystal Light Valve," SPIE Journal on Digital Optical Computing II, Vol. 1215, 314, (1990).
9. R. A. Fisher, ed., Optical Phase Conjugation, Academic Press, New York, NY, 1983.

10. C. S. Tsai, B. Kim and F. R. El-Akkari, "Optical Channel Waveguide Switch and Coupler Using Total Internal Reflection," IEEE Journal of Quantum Electronics, Vol. QE-14, 513, (1978).
11. R. Golshan and J. S. Bedi, "Reversible Nonlinear Interface Optical Computing," Optical Engineering, Vol. 28, 683, (1989).
12. M. Schienle, L. Stoll, G. Schulte-Roth, R. Muller-Nawrath, H. F. Mahlein, R. Marz and C. Cremer, "GaInAsP/InP Zero-Gap Directional Couplers as Compact Optical WDM Filters," Electronics Letters, Vol. 25, 1180, (1989).
13. A. Yariv and P. Yeh, Optical Waves in Crystals, John Wiley and Sons, New York, NY, 1984.
14. D. L. Lee, Electromagnetic Principles of Integrated Optics, John Wiley and Sons, New York, NY, 1986.
15. R. A. Forber and E. Marom, "Symmetric Directional Coupler Switches," IEEE Journal of Quantum Electronics, Vol. QE-22, 911, (1986).
16. M. J. Robertson, S. Ritchie and P. Dayan, "Semiconductor Waveguides: Analysis of Optical Propagation in Single Rib Structures and Directional Couplers," IEE Proceedings, Vol. 132, Pt. J, 336, (1985).
17. G. E. Betts and W. S. C. Chang, "Crossing-Channel Waveguide Electrooptic Modulators," IEEE Journal of Quantum Electronics, Vol. QE-22, 1027, (1986).
18. M. Papuchon and Am. Roy, "Electrically Active Optical Bifurcation: BOA," Applied Physics Letters, Vol. 31, 266, (1977).

19. K. Goel and W. S. C. Chang, "Extinction Ratio Degradation Due to Asymmetry in Zero-Gap Directional Coupling and Crossing Channel Switches," IEEE Journal of Quantum Electronics, Vol. QE-23, 2216, (1987).
20. K. Goel and W. S. C. Chang, "Design Considerations for Crossing Channel Switches," IEEE Journal of Quantum Electronics, Vol. QE-25, 47, (1989).
21. K. Goel, E. Wooten and W. S. C. Chang, "Design Considerations for Low Switching Voltage Crossing Channel Switches," Journal of Lightwave Technology, Vol. 6, 881, (1988).
22. R. A. Forber and E. Marom, "Optimization of Symmetric Zero-Gap Directional Couplers for Large Switch-Array Applications," Conference of Lasers and Electro-Optics Technology Digest, 288, (1985).
23. S. Gevorgyan and A. Hovsepyan, "Power Distribution in Symmetric Integrated Optic X Junction," Electronics Letters, Vol. 26, 788, (1990).
24. A. Neyer, "Electro-Optic X-Switch Using Single-Mode Ti:LiNbO₃ Channel Waveguides," Electronics Letters, Vol. 19, 553, (1983).
25. F. Rottmann, A. Neyer, W. Mevenkamp and E. Voges, "Integrated-Optic Wavelength Multiplexers on Lithium Niobate Based on Two-Mode Interference," Journal of Lightwave Technology, Vol. 6, 946, (1988).

8.0 OPTICALLY RECONFIGURABLE SUPERCONDUCTIVE CIRCUITS

There are two broad categories of optically reconfigurable superconductive devices. One category involves modification of the electrical conductivity of the superconductivity locally, i.e., making local regions nonsuperconducting. The other category involves modification of the magnetic state of the superconductor, i.e., making local regions magnetic or removing existing magnetism. In both cases, the localized flux modifications can result in a defined "filter function." By a filter function one means any kind of bandpass, variable delay line, or weighted distributed processor.

The embodiments of the two reconfigurable approaches are presented in AF Invention 19320 and AF Invention 20631. AF Invention 1320 is entitled "Superconducting Optically Reconfigurable Electrical Device" and is letters patent, United States Patent Number 5,258,626. AF Invention 20631 is entitled "Optically Reconfigurable Magnetic Device" and is letters patent, United States Patent Number 5,287,302.

The invention relates to the field of superconducting materials and to thin film geometries of these materials which are alterable through the use of controlling, spatially distributed optical energy.

The "electrical" device is based on the ability of the superconductor to transition from a non-resistive to a resistive state utilizing optical radiation. Optical radiation has two mechanisms to achieve this transition; namely, through localized heating to above the transition temperature, and through localized breaking up of "Cooper" electron pairs, i. e., quasiparticles. Cooper pair density can also be changed through other means such as electron injection.

The "magnetic" device is based on the ability of a superconductor to maintain its localized magnetic state, i. e., the Meissner effect. The Meissner effect is the phenomena of maintaining the existent magnetic state of the superconductor locally as the local temperature changes from the resistive to the non-resistive, i. e., superconducting, state. With a "ferroelectric" material in proximity to the magnetism of the superconductor the local effective dielectric constant is varied. As the effective dielectric state is varied, coupling between adjacent conductors will vary.

It should be noted that the "magnetic" device only requires the Meissner effect. Consequently, the complete material need not be contiguously superconducting. Therefore, the materials which have some components superconducting can be utilized for the "magnetic" device. Since the "partial" superconductors have "appeared" at temperatures well above 200 °K, operation with thermoelectric coolers is a distinct possibility. Such operation greatly increases the potential utility and application of the phenomena.

Completion of conclusive experimental effort was not achieved due to the reassignment of personnel and limited in-house budget.

8.1 The Reconfigurable Electrical Device

The superconducting optically reconfigurable device (SORD) is based on the use of superconducting transmission lines. The most desirable mechanism of change is quasiparticle injection via optical energy, since, that mechanism is a subnanosecond phenomena. The less desirable bulk thermal change can achieve the same thing but with the characteristic thermal response times. In addition, a bulk thermal change increases significantly the load on the cryogenic refrigeration required to maintain the requisite superconducting critical temperature.

By changing the optical illumination pattern on a transmission line, one effects a change in the local impedance pattern. A spatially varying impedance pattern is the core concept behind distributed element transmission line filters. Therefore, a change in the spatial pattern is a change in the filter function.

There are two varieties of superconductors which are termed Type I and Type II. The differences between the two is the phase transition characteristics between normal and superconducting phases. Figures 8-1 and 8-2 illustrate Type I.

Figures 8-3 and 8-4 illustrate Type II. The Meissner effect provides a description of the differences between the two. As a Type I superconductor transitions from the normal to the superconducting state, any magnetic field entering the material will be locked in during the phase transition. In a Type II superconductor, prior to phase transition, there is a partial penetration of magnetic flux into the mass of the superconductor. The Meissner effect is manifest by the expulsion of magnetic flux from the interior when the superconductor is in the superconducting state. Type II superconductors are referred to as "hard" because of magnetic flux "pinning," i.e., stable flux vortices.

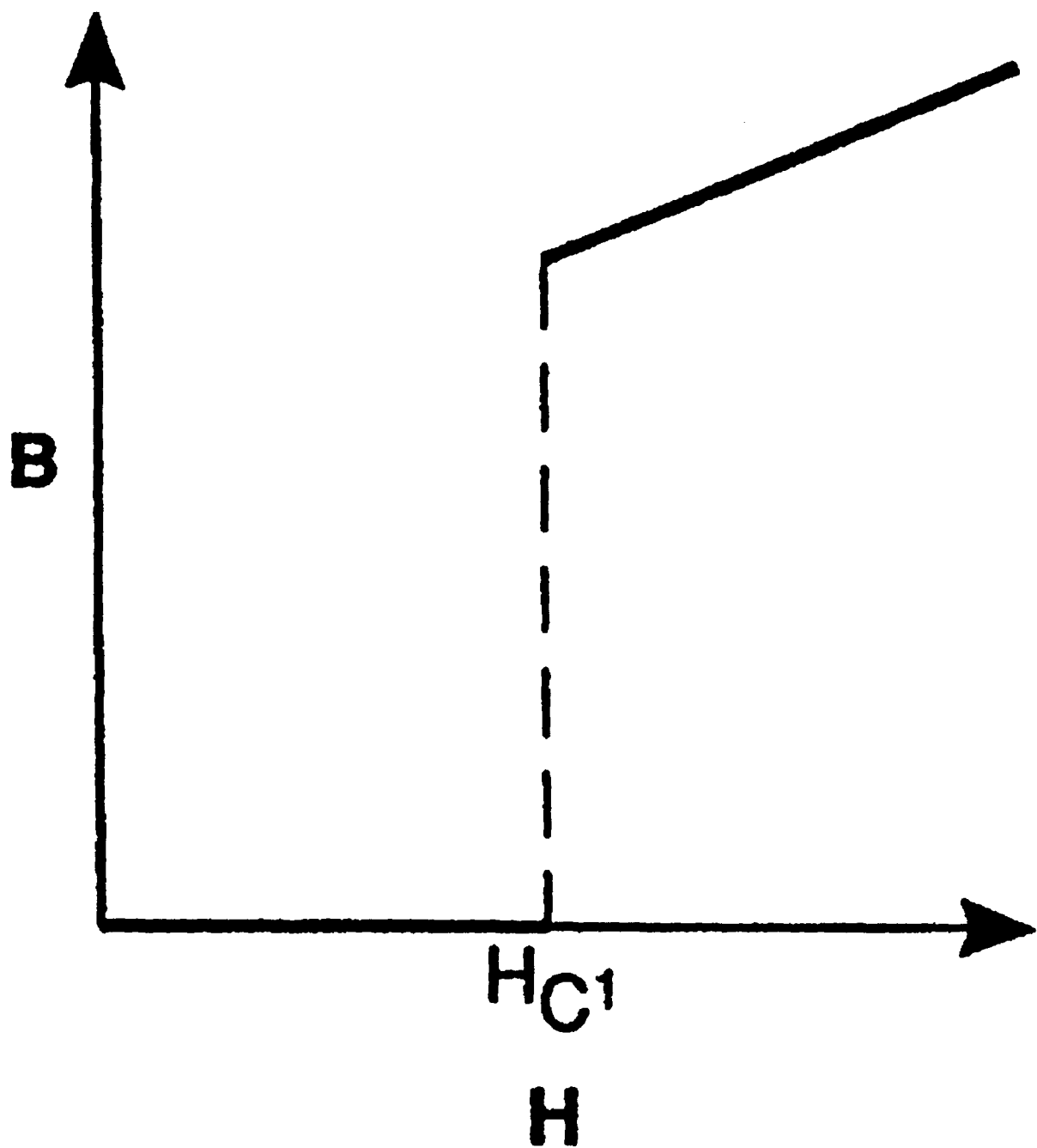


Figure 8-1: Typical Type I Superconductor B Versus H Curve.

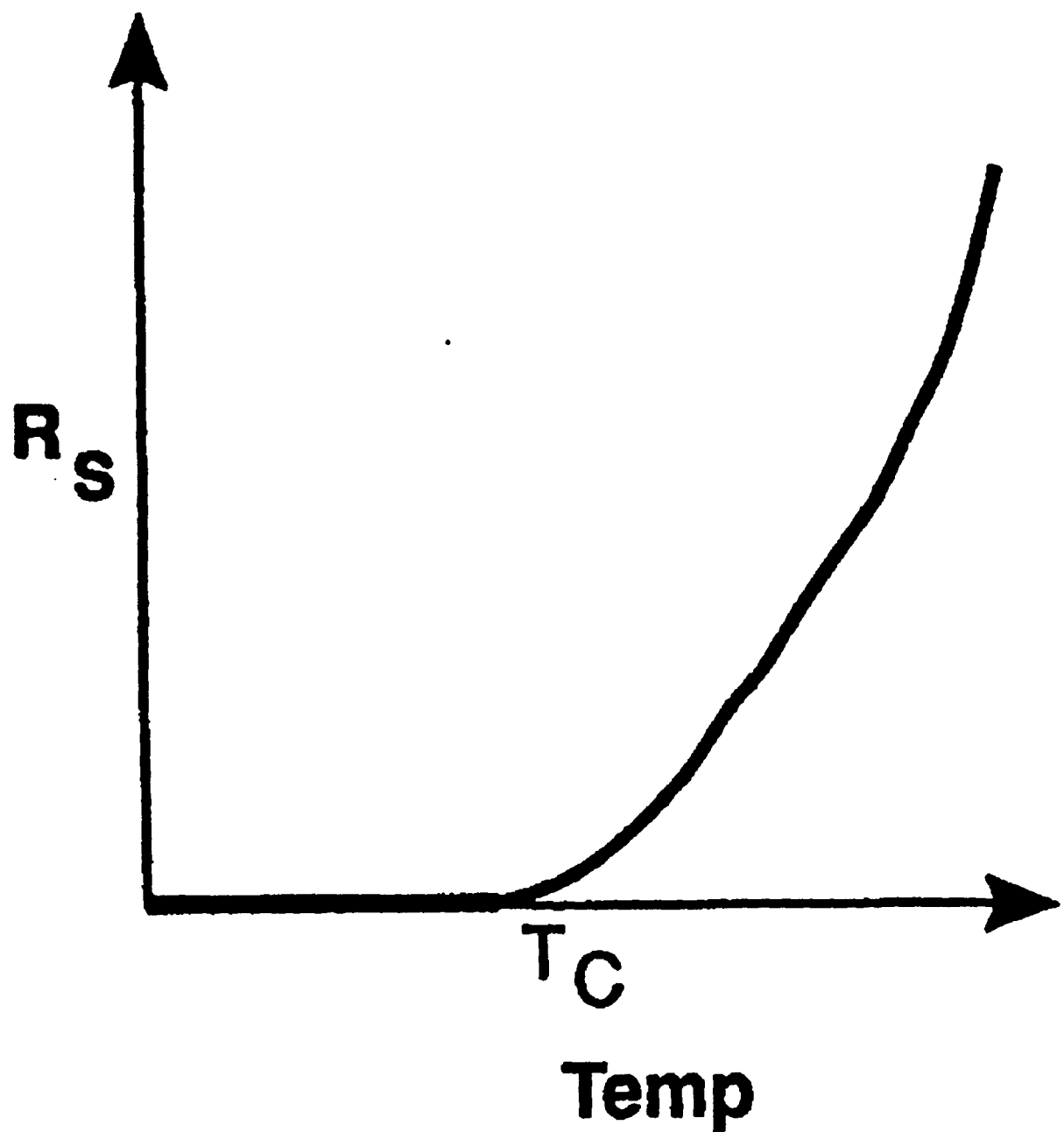


Figure 8-2: Illustration of a Representative R_s Versus Temperature for a Type I Superconductor.

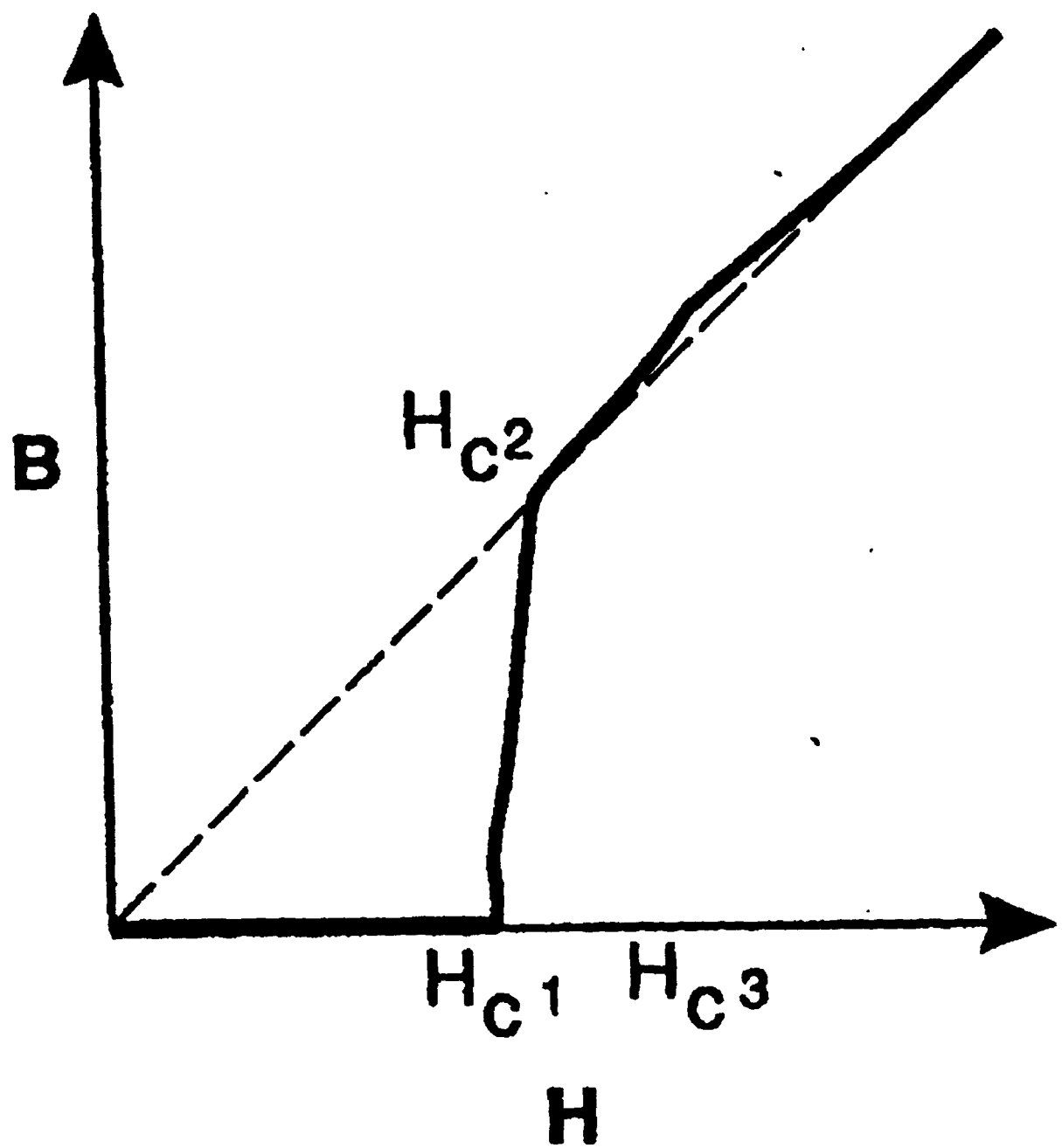


Figure 8-3: Typical B Versus H Curve for a Type II Superconductor.

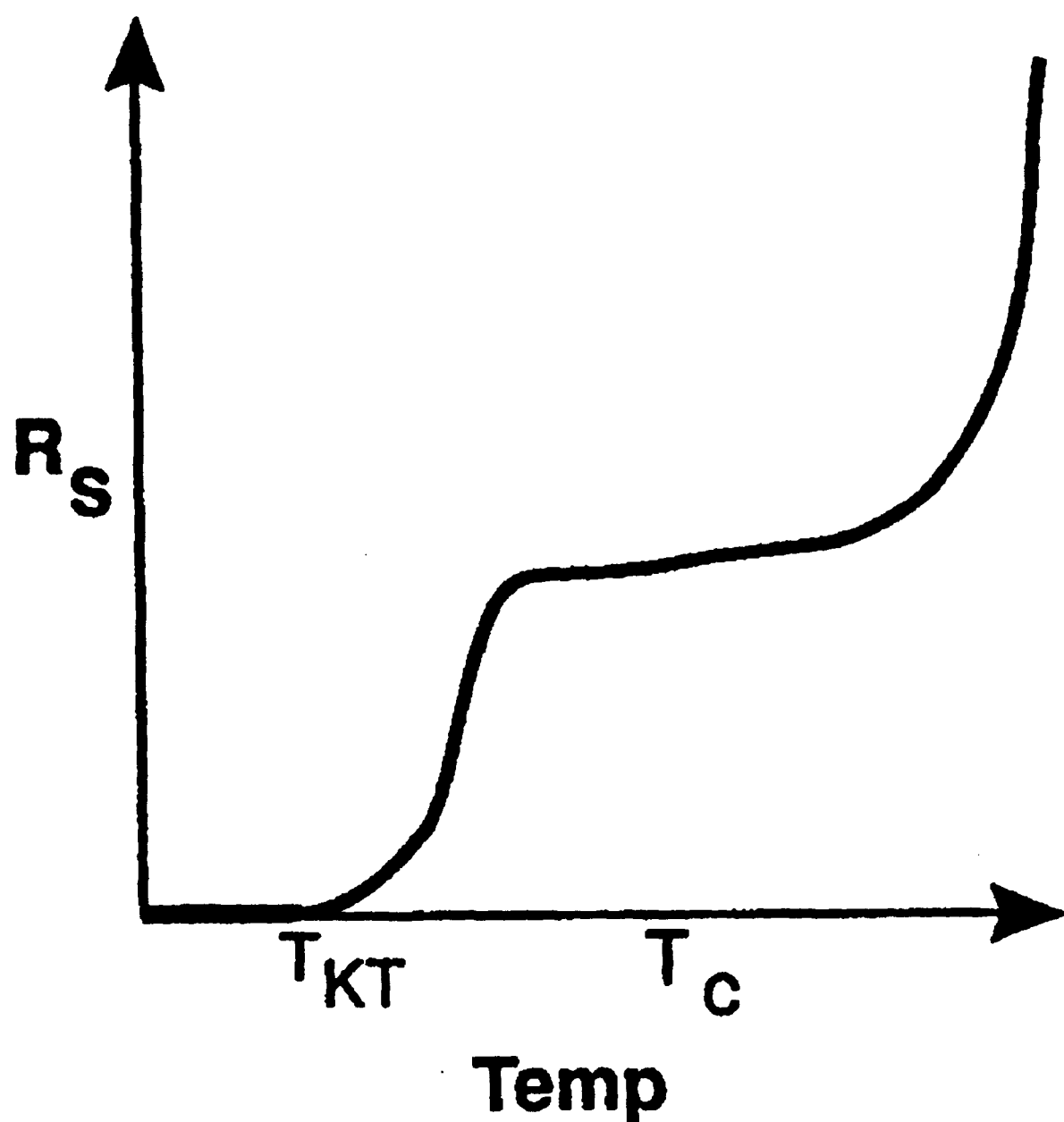


Figure 8-4: Illustration of a Typical R_s Versus Temperature Curve for a Type II Superconductor.

When a superconducting film exhibits a thermal transition, such as from optical illumination, the heat transfer model is appropriate:

$$T = 1.18 F (\tau / (Kcp))^{3/2} \quad (8-1)$$

where T is the change in temperature, τ is the duration of the optical pulse, F is the rate of heat supplied, K is the substrate thermal conductivity, c is the substrate specific heat, and p is the substrate density. If one utilizes a 1.06 μm Nd:YAG laser pulse with a 200 nanosecond Gaussian pulse of 16 nanojoules/cm² on YBCO, the YBCO will undergo a rise in temperature of 1.7°K.

By selectively masking and illuminating parts of a superconducting transmission line, those illuminated parts can undergo the requisite phase transition. If we utilize a microstrip line, we note that it operates as a quasi-transverse electromagnetic mode (-TEM) device. Therefore, one can use the static TEM parameters to define the sine parameters. This assumption is valid for frequencies less than 20-30 GHz. A more complex model is required above those frequencies. For our purposes, the distributed parameters, i. e., per unit, can be modeled:

$$R_s = (\omega^2 \mu \lambda^3 / 2) (T_c/T) (e^{-(\Delta T / (k_b T))}) \quad (8-2)$$

$$\Delta T \approx 3.2 k_b T_c (1 - T/T_c)^{1/2} \quad (8-3)$$

$$L = (h\mu/KW) \{(1 + \lambda_1/h') \coth(t_1/\lambda_1)\} \{(\lambda_2/h) \coth(t_2/\lambda_2)\} \quad (8-4)$$

$$\lambda_L(T) = \lambda_L(0) [1 - (T/T_c)^4]^{-1/2} \quad (8-5)$$

$$C = \epsilon K W / d \quad (8-6)$$

$$\epsilon = \epsilon_0 \epsilon_{eff} \quad (8-7)$$

$$G = \sigma W / d \quad (8-8)$$

Where ω is the angular frequency in (radians/sec), μ is the permeability (H/m), ϵ is the permittivity (F/m), λ is the penetration depth (m), T is the ambient temperature ($^{\circ}$ K), K is a geometric factor, k_b is Boltzman's constant (J/ $^{\circ}$ K), σ is the electrical conductivity (0, mohs), h (and d) is the separation of the superconductors, t_i is the thickness of the superconductors, and w is the width of the stripline.

For thin films $t_i \ll \lambda_i$ so, $\coth(t_i/\lambda_i) \approx (\lambda_i/t_i)$ and $L = (h\mu/KW)(1 + \lambda_1^2/ht_1 + \lambda_2^2/ht_2)$.

For thick films $t_i \approx \lambda_i$ so, $\coth(t_i/\lambda_i) \approx 1$ and $L = (h\mu/KW)(1 + \lambda_1/h + \lambda_2/h)$.

Whenever permittivity is referred to, it is a function of the effective dielectric constant. The effective dielectric constant is bounded by the value of the aspect ratio defined as the ratio of the film width (W) to dielectric thickness. In which case, for $W > h$, $\epsilon_{eff} = \epsilon_r$; and for $W < h$, $\epsilon_{eff} = (1/2)(\epsilon_r + 1)$.

The geometrical factor is used to compensate for fringing field effects encountered in stripline devices. The geometrical factor depends on the aspect ratio as well as the thin film thickness to separation ratio. The geometric parameter is independent of the material, but, it directly impacts impedance and capacitance. As the aspect ratio decreases and the film thickness increases, the fringing field effect becomes more significant as shown in Figure 8-5.

The distributed system parameters are derived from the basic 2-fluid London model for superconductors except for the definition of surface resistivity which is derived from the Bardeen, Cooper, and Schrieffer model. The surface resistivity also needs to take into account a residual resistivity factor (R_{res}) which is dependent upon density of impurities and trapped flux. When the residual resistivity factor is incorporated into the surface resistance

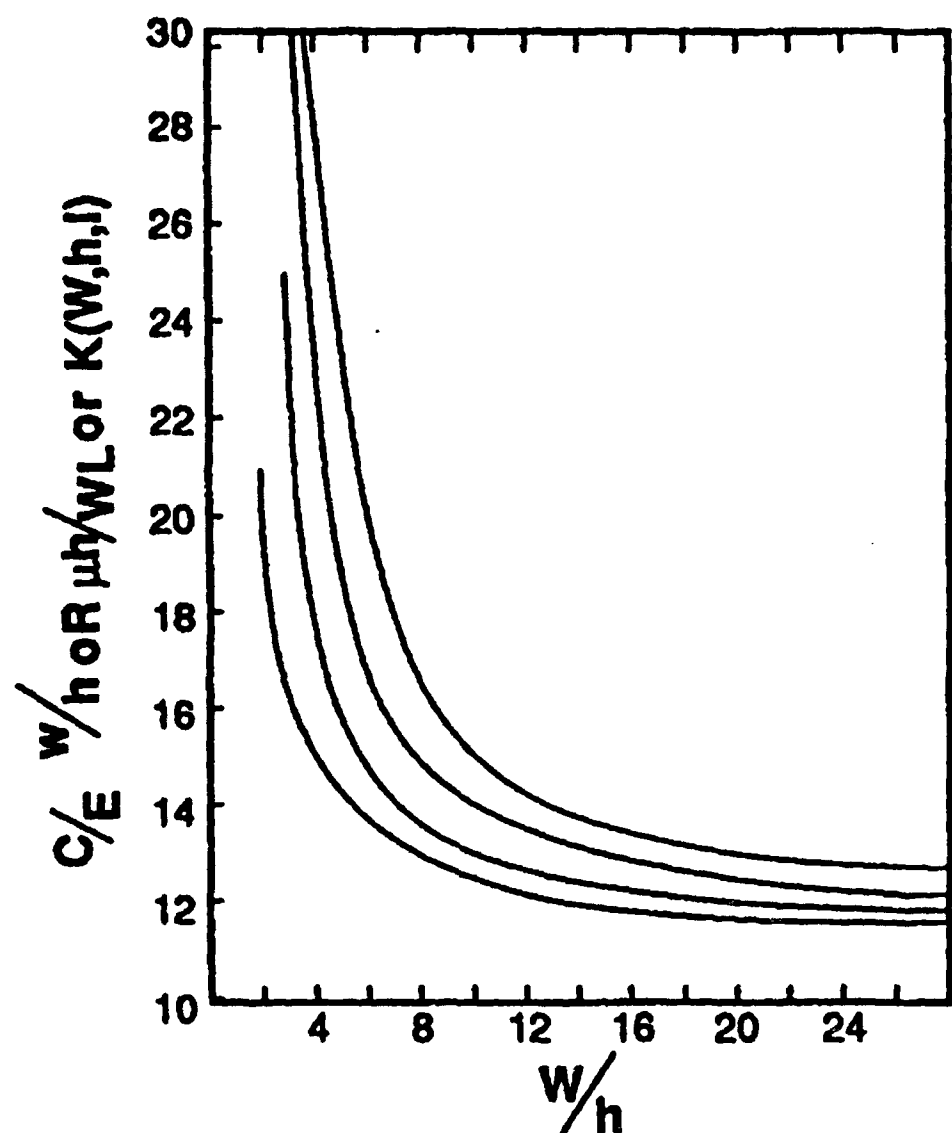


Figure 8-5: Illustration of Fringing Field Effects As Seen In a C/E versus W/h curve.

calculation, the theoretical and empirical results are in basic agreement.

Once the distributed line parameters have been defined, the standard microstrip line impedance (Z_0) and propagation constant (γ) follow:

$$Z_0 = [(R+j\omega L)/(G+j\omega C)]^{1/2} \quad (8-9)$$

$$\gamma = [(R+j\omega L) * (G+j\omega C)]^{1/2} \quad (8-10)$$

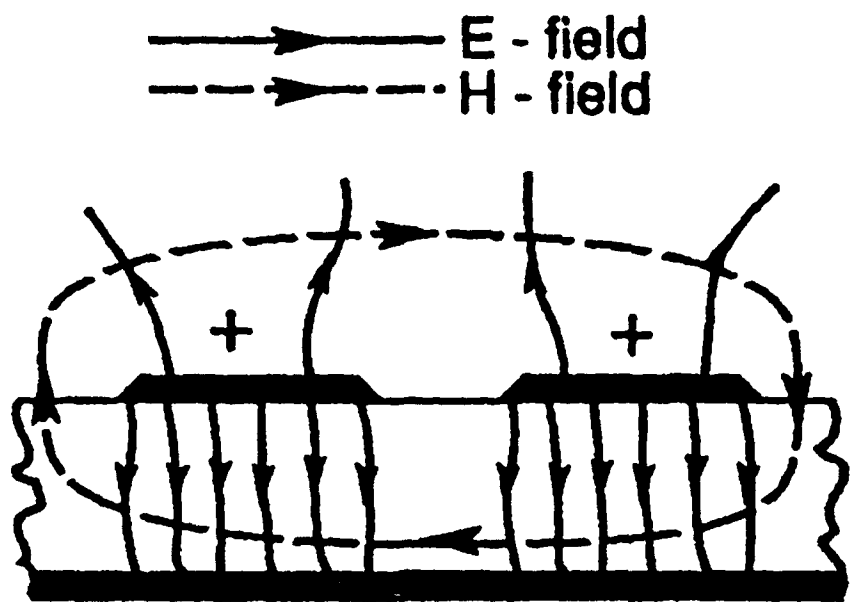
If the superconducting line is in the low loss region, i.e., R and G are small, then $Z_0 = (L/C)^{1/2}$ and the phase constant $\beta = \omega(LC)^{1/2}$.

One can define the velocities of phase as $v_p = \omega/\beta = 1/(LC)^{1/2}$ and of group as $v_g = d\omega/d\beta$.

The total time delay of the transmission line is the ratio of the line length and group velocity, i.e., $t_d = \text{line length}/v_g$.

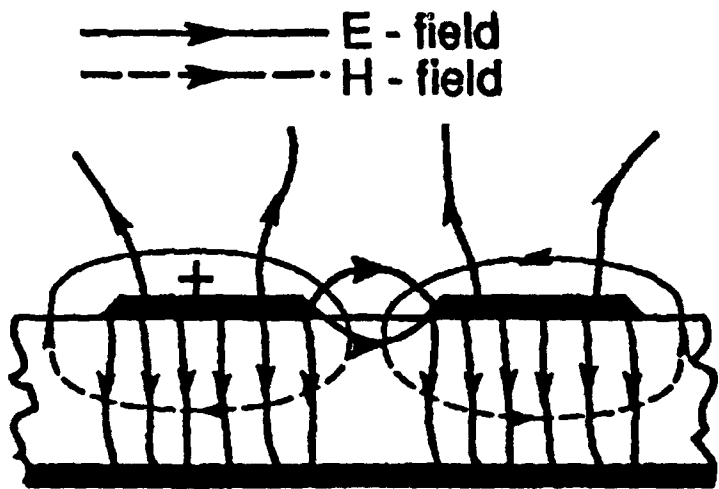
Coupling of microstrip transmission lines is generally capacitive in nature. The nature of the capacitance depends on whether the prevailing field structure is even (e) or odd (o). See Figures 8-6 and 8-7.

The fields are given by $C_e = C_p + C_{fe} + C_f$ and $C_o = C_p + C_{fe} + C_{ga} + C_{gd}$. Where C_p is associated with the parallel plates, C_{ga} and C_{gd} are line to line coupling in air and medium respectively while C_{fe} is the line to line coupling associated with the magnetic link, and C_f is associated with fringing. See Figures 8-8 and 8-9. For the development here, we have $C_p = \epsilon_0 \epsilon_r (W/h)$, $2C_f = [(\epsilon_{eff})^{1/2}/cZ_0] - C_p$, and $C_{fe} = [C_f / \{1 + (Ah/s)\tanh(8s/h)\}] [\epsilon_r / \epsilon_{eff}]^{1/2}$ where, $A = \exp\{-[0.1e^{(2.33-2.53W/h)}]\}$. The capacitance across the dielectric is $C_{gd} = [\epsilon_0 \epsilon_r / \pi] [\ln(\coth(\pi s/4h))] + 0.65C_f[((0.02h/s)\sqrt{\epsilon_r}) + 1 - \epsilon_r^{-2}]$, and through the air is $C_{gs} = \epsilon_0 [K(k')/K(k)]$, $k = (s/h) / [(s/h) + (2w/h)]$, with $k' = (1-k^2)^{1/2}$, $[K(k')/K(k)] = (1/\pi) [\ln(2(1+k'^{1/2})/(1-k'^{1/2}))]$. Which, for $0 \leq k^2 \leq 0.5$ has $[K(k')/K(k)] = \pi / [\ln(2(1+k^{1/2})/(1-k^{1/2}))]$.



Even Mode

Figure 8-6: Illustration of Field Pattern for Dual Microstrip Line Showing Even Mode Distribution.



Odd Mode

Figure 8-7: Illustration of Field Pattern for Dual Microstrip Line Showing Odd Mode Distribution.

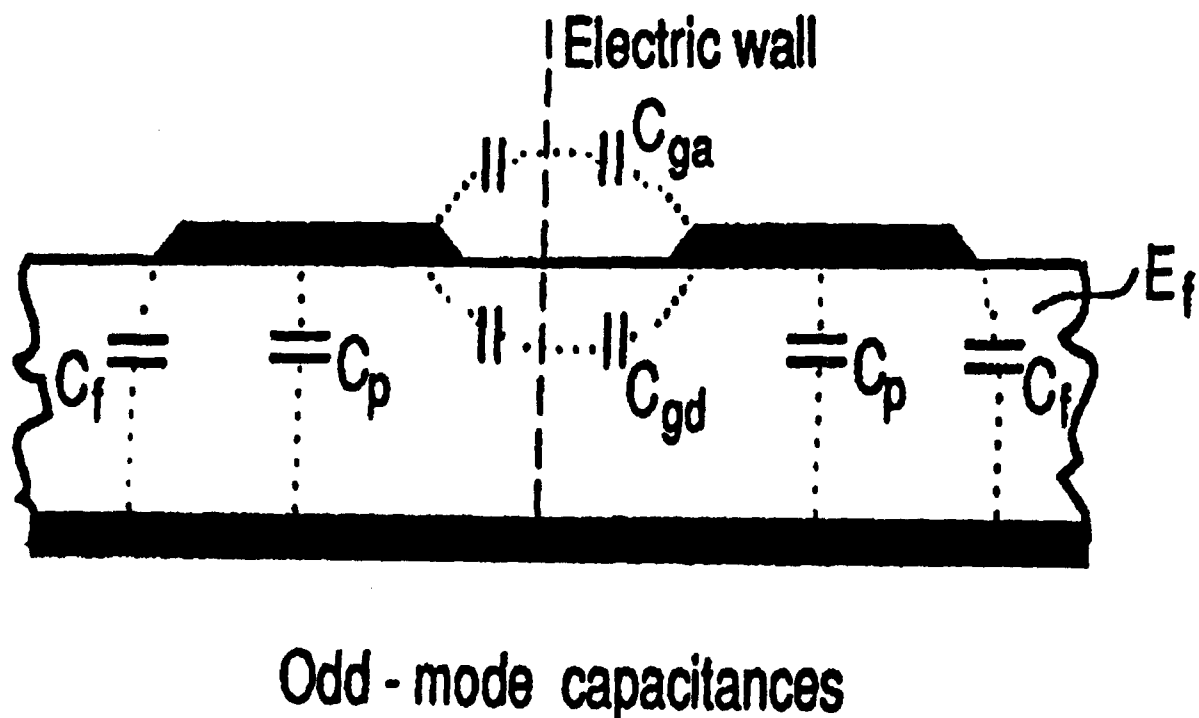
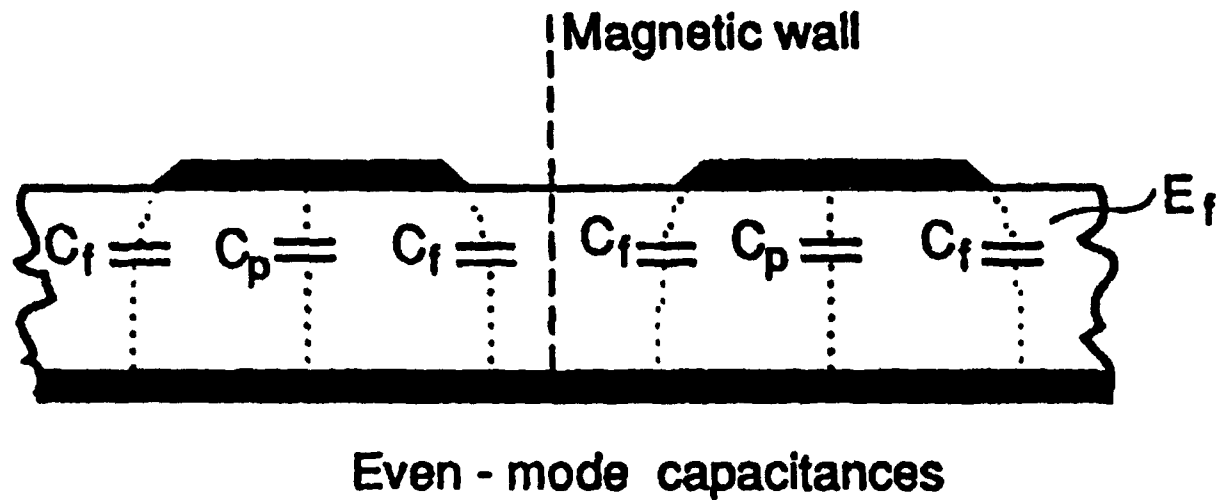


Figure 8-9: Illustration of Odd Mode Capacitances for a Dual Transmission Microstrip.

Using the definitions for the odd and even mode capacitances the characteristic impedances become:

$$Z_{0o} = 1/(cC_{lo}E_{effo})^{1/2} \quad (8-11)$$

$$Z_{0e} = 1/(cC_{le}E_{effe})^{1/2} \quad (8-12)$$

Therefore, $C = (Z_{0e}-Z_{0o})/(Z_{0e}+Z_{0o})$.

A typical backward wave coupling structure is shown in Figure 8-10, for which the terminal voltages are defined by $V_1 = 1$, $V_2 = (1-C^2)^{1/2}/\{1-C^2(\cos\theta + j\sin\theta)\}^{1/2}$, $V_3 = j\sin\theta/\{1-C^2(\cos\theta + j\sin\theta)\}^{1/2}$, and $V_4 = 0$.

The forward coupled voltage is assumed to be negligible, however, there will be some forward voltage transfer. The backward coupled voltage at terminal 3 is used to define the length l_g at which the maximum signal is coupled. This length is wavelength dependent and forms the basis of the filter functions.

$$l_g = \lambda_g/\{4(2n-1)\} \text{ for } n = 1, 2, 3, \dots \quad (8-13)$$

At this point the standard filter function equations can be used to define the desirable length and width sequences for each response desired. The length and width in turn define the required "mask" or write area for the light to convert the superconductor to a non-superconducting region.

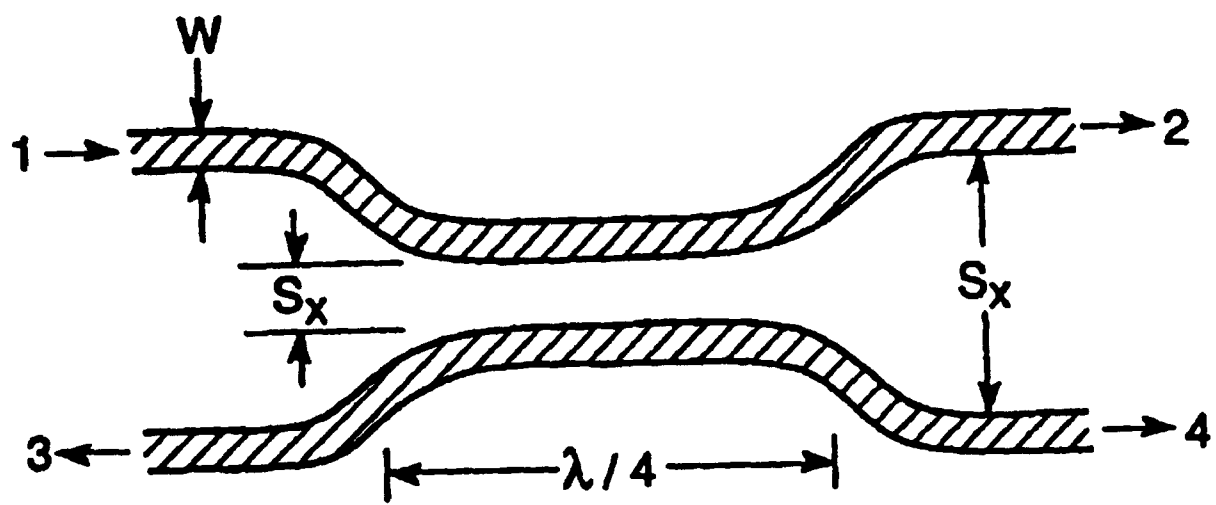


Figure 8-10: Illustration of a Dual Transmission Microstrip Backward Wave Coupling Structure.

8.1.1 General References

- I. Bozovic, et al., Phys Rev Lett. 59 2219 (1987).
- W. R. Donaldson, et al., Appl. Phys. Lett. 54 24 (12 June 1989).
- H. S. Kwok, et al., Appl. Phys. Lett. 54 124 (12 June 1989).
- P. B. Corkum, et al., Phys. Rev. Lett. 61 2886 (1988)
- H. S. Carslaw and J. C. Geager, Conduction of Heat in solids (Clarendon, Oxford) 1986.
- A. Frenkel, et al., Appl. Phys. Lett. 54 16 (17 Apr. 1989).
- T. C. Edwards, Foundation of Microstrip Design (John Wiley & Sons, New York) 1981.
- T. Van Duzer and C. W. Turner, Principles of Superconductive Devices and Circuits (Elsevier, New York) 1981.
- W. H. Chang, J. Appl. Phys. 50 24 (Dec. 1989).
- S. M. Anlage, et al., Appl. Phys. Lett. 54 204 (26 June 1989).
- R. S. Withers, et al., IEEE Trans. Mag. MAG-19 (3) 480-484 (1983).
- C. E. Cook and M. Bernfeld, Radar Signals (Academic Press, New York) 1967.
- R. N. Bates and R. E. Pearson, Electronic Engineering p. 39-41, (April 1978).
- G. L. Matthaei, et al., Microwave Filters, Impedance-Matching Networks, and Coupling Structures (McGraw-Hill, New York) 1964.

8.2 The Reconfigurable Magnetic Device

The significant change from the electrical device is emphasis on the utilization of the Meissner effect. The ability to exclude or maintain a magnetic field as a function of the prior superconductor phase history permits local control of "magnetic" memory. So long as the superconductor does not change phase again, the optically controlled magnetic domains will remain in their current state. As in Section 8.1, light can be utilized to spatially write phase change regions. If one has in proximity to the superconductor a "Faraday effect" type material or other material whose degree of magnetism can be observed, one can determine the local states magnetic field. Therefore, one has a memory mechanism. It is to be noted that the "trapped" phase information disappears when the superconductor material is raised above its critical temperature.

If one has two or more superconductors in proximity to each other and between those superconductors is a medium whose permeability is a function of the local magnetic field, one can control the degree of coupling between the lines by affecting a local phase change, i. e., cycling through the transition temperature, in the presence or absence of a magnetic field.

If one constructs a multiple transmission line similar to that indicated in Figure 8-11, one can realize the equivalent of an interdigitated surface acoustic wave filter (SAW). The difference from the SAW filter is that the coupling characteristic is controlled by the presence of a local magnetic field which influences the permeability or permitivity locally.

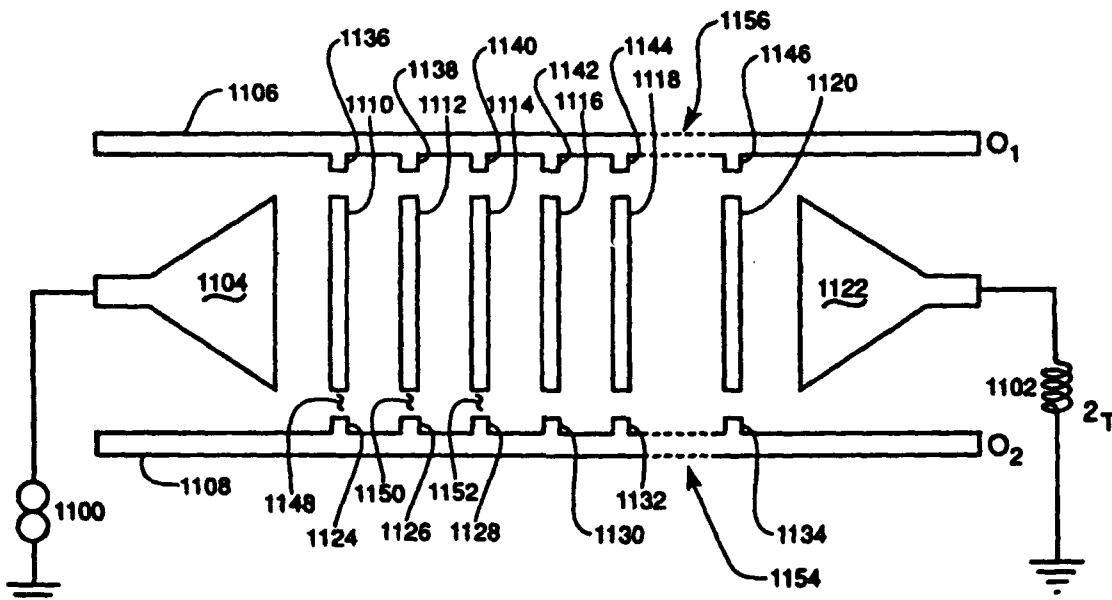


Figure 8-11: Illustration of a Coupled Wave Transmission Line With "Interdigitated" Coupling.

The SAW filters are part of the larger category of transversal filters. With the recognition that the weights of the interdigitated areas correspond to the weights of a SAW filter and the slow traveling wave nature of the adjacent conductors, one can readily design the filters using standard theory. The reader is referred to the standard works of the following for reference:

R. A. Waldron, Ferrites, An Introduction for Microwave Engineers, (D. Von Nostrand Co., New York 1961).

Supriyo Datta, Surface Acoustic Wave Devices, (Prentice Hall, New York, 1986).

J. D. Kraus, Electromagnetics, (McGraw-Hill, New York 1953).

Colin Campbell, Surface Acoustic Wave Designs & Their Signal Processing Applications, (Academic Press, New York, 1989).

9.0 INITIAL INVESTIGATION OF AOTF & FOBG

The purpose of this research effort was to determine the limitations of an amplitude modulated (AM) Acousto-Optical Tunable Filter (AOTF) when used as a spectrum analyzer with multiple drive frequencies for multiple channels. Spectrum analysis is used to determine the reflected wavelength from the Fiber Optic Bragg Grating sensor. Until this investigation, the behavior of a multiple channel AM AOTF has not been studied. Multiple AM channels has the potential advantage of making them electronically separable and minimizing the number of optical sources and sensors.

Optical fibers are being widely used for communications because of their long distance transmission capability and immunity to electromagnetic interference. During the past 15 years optical-fiber sensors have been under development. In a fiber sensor, a beam of light which is sent through the fiber(s) can be used to determine the localized properties of the fiber. When the effective length, or birefringence is modified, due to an external force, this length can be determined by the time of travel or wavelength reflectivity (for Bragg grating based sensors. The applications of these sensors range from stress and temperature monitoring to process control of flow, pressure, and liquid level in industrial systems. One application is in "smart structures" for distributed strain and temperature sensing of aircraft. In the smart structures concept, the fibers are embedded in the structure to be monitored.

The technique most extensively utilized at this time for strain measurements is based on using phase interference techniques. There is no residual memory in such techniques, and they detect the strain along the total length of the fiber. These techniques detect the change in the optical path, i.e., strain, only while the measurement system is running. Any strain developed while the

measurement system is not running will not be detected. Therefore, the cumulative stress on the structures lifetime cannot be measured, unless the measurement system is running. In addition, two fibers of equal length are needed, one being the sensing fiber and the other the reference fiber.

The fiber optic Bragg grating sensors is an approach to solve these problems. With this type of sensor, strain and temperature can be monitored in a localized region of the optical fiber. In addition, the cumulative strain and temperature change that occurs while the measurement electronics is not running can be determined. The measurement system investigated in this research is based on an AOTF. The AOTF is compact and rugged. In addition, it can potentially operate multiple channels simultaneously and independently.

9.1 Background on Diffraction

In 1978, Hill and coworkers discovered that narrow bandwidth Bragg gratings could be created within the germanium-doped core of certain optical fibers using green light as can be realized with an argon ion laser. This photosensitivity has been observed to be even stronger when ultraviolet light is used to irradiate the optical fiber. The Bragg gratings result from a periodic variation of the refractive index between 10^{-5} and 10^{-4} along the fiber core. These intra core gratings are written by sideways exposure of the core to ultraviolet light in the form of an interference pattern. These gratings form the basis of an important new class of optical sensors. However, the lack of a compact and rugged system that can rapidly determine this bragg wavelength has severely limited the use of the intracore Bragg gratings as practical sensors.

The mathematical model of acousto-optic diffraction is similar to that of a transmission diffraction grating. As such, it is possible to use an acousto-optic Bragg cell as the dispersive element in an optical spectrometer. In a diffraction grating a repetitive array of elements, see Figure 9-1, has the effects of producing periodic alteration in the phase, amplitude, or both on an emergent wave. The diffraction grating acts similar to a prism diffracting light of different wavelengths at different angles.

The distance between the elements in a diffraction grating is known as the grating constant, parameter a in Figure 9-1. In the acousto-optic grating, the grating constant is equal to the acoustic wavelength. One obvious advantage of an acousto-optic grating spectrometer is that the grating constant can be changed electronically by changing the rf drive frequency, thus, providing a capability of rapidly scanning the spectral region at an observation point. As for a single detector diffraction grating spectrometer the diffraction grating has to be physically rotated to produce a scan of the spectral region of interest.

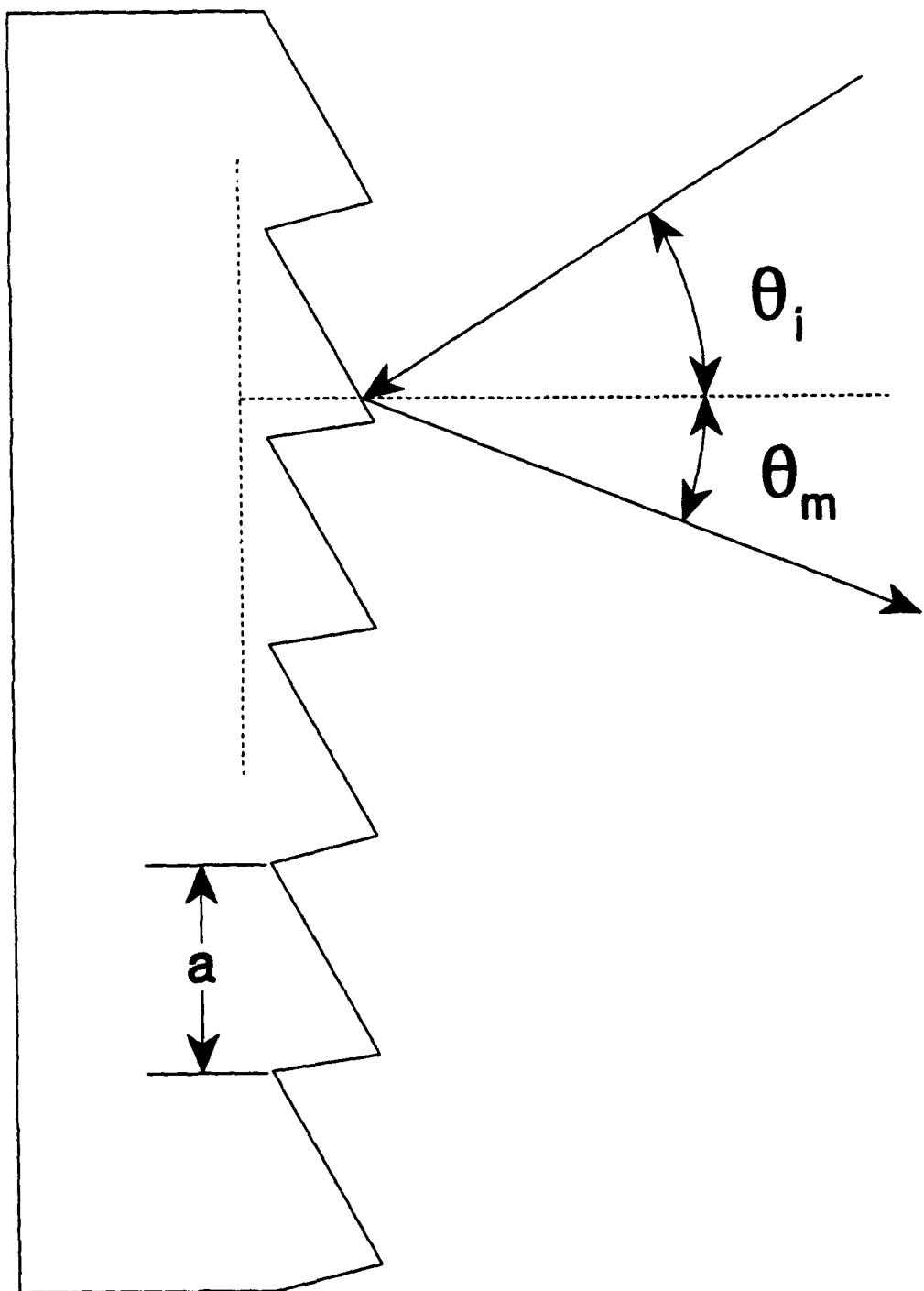


Figure 9-1: Section of a Reflection Grating.

To minimize the mechanical movement, a linear array of detector elements can be used, resulting in a faster scan of the region covered. In a values, are determined by a , λ , and θ_i , and is given by the equation:

$$a(\sin\theta_m - \sin\theta_i) = m\lambda \quad 9-1$$

where θ_m and θ_i are measured from the normal of the grating plane and not with the individual groove surfaces.

In a typical single detector diffraction grating spectrum analyzer, light is collimated onto a holographic or ruled grating by a curved mirror. A reflection grating with groove spacing, a , will disperse the incident light into a series of angles, θ_m , according to Equation 9-1.

9.2 Acousto-Optical Tunable Filter (AOTF)

The AOTF is based on acoustic diffractions of light in an anisotropic medium. The device consists of a piezoelectric transducer bonded to a birefringent crystal. When the transducer is excited by an applied RF signal, acoustic waves are generated in the crystal. The propagating acoustic wave produces a periodic modulation of the index of refraction. This provides a moving phase grating, which establishes the anisotropic Bragg diffraction mechanism, that, under proper conditions, will diffract portions of an incident light beam. This anisotropic diffraction involves rotation of the polarization plane of the diffracted wave. For a fixed acoustic frequency, only a limited band of optical frequencies can satisfy the phase-matching condition and produce a maximum intensity while non-phase-matched produce a minimum intensity. As the RF frequency is changed, the center of optical passband is changed accordingly so that the phase-matching condition is maintained. An advantage of the AOTF is the fact that multiple RF frequencies can be used to establish a complex grating pattern within the crystal. This will diffract multiple bands of light corresponding to the multiple RF frequencies.

Being an anisotropic acoustic (as well as optical) material there will be harmonics created which might diffract additional bands and create noise. The detection of light is not a linear process, therefore, there will be additional harmonics created when the signal is amplitude modulated. AM related harmonics will also create noise which will affect the determination of the peak wavelength.

With the theory in mind, an experiment will be designed. The results of the work will be compared with a fully developed theoretical model. Further work on this topic will be reported under work unit 20010512 for project element 62204F.